2018

Two-photon laser-induced fluorescence in sodium-doped composite propellant flame

Keke Zhu
Iowa State University

Two-photon laser-induced fluorescence in sodium-doped composite propellant flame

by

Keke Zhu

A thesis submitted to the graduate faculty

in partial fulfillment of the requirements for the degree of

MASTER OF SCIENCE

Major: Mechanical Engineering

Program of Study Committee:
James Michael, Major Professor
Travis Sippel
Jigang Wang

The student author, whose presentation of the scholarship herein was approved by the program of study committee, is solely responsible for the content of this thesis. The Graduate College will ensure this thesis is globally accessible and will not permit alterations after a degree is conferred.

Iowa State University

Ames, Iowa

2018

TABLE OF CONTENTS

Page

LIST OF FIGURES

Page

LIST OF TABLES

Page

ACKNOWLEDGMENTS

I would like to express my most sincere gratitude to my advisor, Dr. James Michael, for his guidance and patience throughout my study and research at Iowa State University. His creative insights, desire for perfection and incredible love of research inspired me to pursue higher goals in my work. I have benefited from the discussions and become a critical thinker.

I sincerely thank my committee members, Dr. Travis Sippel and, Dr. Jigang Wang for their support and guidance throughout the duration of my graduate research and studies. I also want to thank Dr. Terry Meyer for giving me the opportunity to join his group and meet Dr. Michael before he left for Purdue.

I also appreciate support, assistance, and friendship of my colleagues in the Michael group and Sippel group: Stuart, Chloe, Anthony, Abhijeeb, Mark, and Jordan. Thanks for all the friends I met in Ames.

Finally, I am grateful for my parents, for their love and support.

This research was supported by Air Force Office of Scientific Research (AFOSR).

ABSTRACT

Alkali metal dopants are common in coal combustion environments, biomass reforming for fuel, and have applications as dopants in combustion for diagnostics and plasma-based control approaches. Recently, alkali-doped solid propellant flames have been demonstrated for enhancing burning rate using continuous microwave-based plasma enhancement, where sodium has been utilized as an electron donor. The performance of microwave coupled burning propellant flames may be optimized through knowledge of the ground-state sodium distribution. However, these systems exhibit significant particle scattering, gray body emission backgrounds, and high optical density, complicating measurements via laser diagnostics. In this work, to infer the sodium distribution in the propellant flame, a single-photon and two-photon absorption laser-induced fluorescence techniques are applied. Two-photon laser-induced fluorescence is shown to improve laser scattering rejection and fluorescence trapping issues exhibited in resonant single-photon laser-induced fluorescence. The 3s-3d excitation scheme is compared directly with 3s-4d excitation by examining fluorescence, amplified spontaneous emission, and ionization levels in sodium doped flame to optimize laser fluence levels. Significant resonance-enhanced multiphoton ionization and amplified spontaneous emission are presented in two-photon excitation schemes. Two-photon laser-induced fluorescence is applied to ground-state atomic sodium spatial distributions in microwave-coupled solid propellant flames.

CHAPTER 1. INTRODUCTION

1.1 Motivation

Alkali compounds are naturally present in coal, organic matter in biomass-derived fuels[1], and in animal tissue as ingredients[2,3]. In combustion, alkali-content can play a role in reactions with the indigenous sulfur, impurities, and agents are typically added to control sulfur dioxide formation[2]. Alkali metals have also been used in a variety of combustion and high-speed aerodynamic systems. In addition, sodium can either be added to combustion environments for temperature measurements[4], or aerodynamic flow for velocity measurements[5]. Due to the accessibility of sodium D lines and high absorption cross section, sodium is an attractive alkali for these purposes[6]. The low ionization threshold of alkali vapors has also been proposed for a number of plasma-based combustion and flow techniques. One promising application involving the addition of sodium or alkali metal vapors is in magnetohydrodynamic power extraction, where a few percent of sodium or cesium vapor has been proposed to increase the extraction of electrical power from hypersonic flows[86-87]. An additional application of particular interest to the work presented in this dissertation is seeding alkali metal as an electron donor for microwave-assisted combustion and flame speed enhancement due to low ionization threshold.

Solid propellants are used for a variety of propulsion applications. Unlike liquid engines or hybrid rockets[7], which can dynamically control flow rate, control of solid propellant rocket engines is difficult. Moreover, solid propellant burning instabilities can generate unwanted vibration in the engines[8]. Finally, ignition and extinction of solid rocket motors are difficult to achieve in practice. Recently, the microwave-enhanced combustion of alkali-doped solid propellant formulations was shown to enhance burning rates by Barkley et al.[9,10]. The

modification of microwave energy deposition to the flame by changing the doping level of low-ionization threshold alkali metals offers the potential for active control of solid propellant burning.

Nearly all solid propellants are composite mixtures of several ingredients such as oxidizer, fuel, binder, plasticizer, stabilizer and cross-linking agent. The specific chemical composition depends on the desired combustion characteristics for a propellant application. The heterogeneous or composite propellant ingredients include ammonium perchlorate (AP) as oxidizers, hydroxyl-terminated polybutadiene (HTPB) as binder, and aluminum as stabilizer. Solid propellant flames have strong gray body emission, multiphase reactions, complex chemistry reactions, and heterogeneous and time-varying composition[11]. It is necessary to understand the decomposition processes and kinetic mechanisms of the solid propellants to establish models[12]. The development of such models is a significant step towards more accurate and comprehensive predictions, and helps optimize chemical compositions to meet the required needs[13].

Studies on the microwave-throttling of composite propellant formulations with the addition of sodium dopant have identified a complicated set of mechanisms with potential energy addition in the gas phase, the condensed phase of the bulk propellant, and the condensed-phase products present in metalized propellant formulations[9]. In the deposition to the gas-phase of these flames, the hypothesis is that the doping level of sodium is a significant driver in the amount of absorbed energy. In order to better characterize the interaction of the multiphase propellant combustion flame with the microwave field, an improved understanding of the distributions and role of seeded atomic sodium in these systems is required. Detailed investigation of the distribution of atomic sodium distribution relative to the propellant flame

structure is necessary to account for the microwave energy coupling processes in the microwave-enhanced propellant burning.

1.2 Literature Review

Solid propellant combustion exhibits both high temperature and multiphase phenomena, which makes it a challenging environment for study[11]. Due to this fact, laser-based combustion diagnostics have potential as non-intrusive, in-situ, and high resolution (temporal and spatial) measurement techniques to study propellant combustion[14]. Information about the thermodynamic environment, the species distributions, and the phase distributions is helpful for understanding basic combustion processes, and can also be applied to build up detailed numerical models. Several optical techniques have been applied to solid propellant flames, including emission spectroscopy[15,16], absorption spectroscopy[17], Raman spectroscopy[18,19] and laser-induced fluorescence (LIF)[12,20].

For the alkali-metal doped propellant flames we are considering, sodium spectroscopy is a possible candidate for determining local temperature and sodium concentration distribution in the flame. Although single-photon laser-induced fluorescence (LIF) has been successfully applied for temperature and concentration measurements of sodium previously, correction is required in high optical density environments due to the resonant excitation and emission[6,21]. The issue of fluorescence re-emission and particle scattering in the flame cannot be avoided by optical filters.

Alternative methods have been explored in small molecules and atoms using multiphoton laser excitation and subsequent fluorescence. Similar multiphoton techniques have been studied extensively in combustion environments using H atom[22], O atom[23] and the CO molecule[24]. For these atomic systems, two-photon laser-induced fluorescence (TALIF) has the advantage of avoiding fluorescence trapping as compared to single-photon resonance

excitation. To understand the fundamental of sodium TALIF, this work was done by premixed sodium seeded flame, then applied to a propellant flame. It shows the promising way to show the qualitative map of sodium concentration distribution map in the flame environments.

1.3 Objectives

The objectives of this dissertation are three-fold. They include:

1. The qualitative determination of atomic alkali distributions in highly scattering multiphase combustion environments.
2. The qualitative determination of alkali distributions in environments with high number density atomic species and the assessment of quantitative mapping with two-photon laser-induced fluorescence of sodium.
3. The determination of the variation in sodium distributions leading to plasma production and flame enhancement effects in microwave-enhanced propellant flames.

1.4 Summary of Thesis

In this thesis, a two-photon absorption planar laser-induced fluorescence (TALIF) of sodium is detailed. The second harmonic of a 10 Hz nanosecond Nd:YAG laser was used to pump a dye laser to achieve three separate excitation schemes for sodium atomic fluorescence. A one-photon excitation scheme at 589 nm is compared to two-photon excitation schemes at 578 nm and 685 nm in a sodium-seeded gas-phase burner. The use of sodium TALIF schemes in the gas-phase flame showed improved signal trapping characteristics, reduced laser scattering, and allowed signal-to-noise determination for the various excitation schemes.

In sodium-doped propellant flames, improvements in signal-to-noise ratio were realized with 685 nm two-photon excitation and show the capability of mapping alkali atomic concentrations in the highly scattering, high optical density environment of the sodium-doped

propellant flames. TALIF images of microwave-coupled sodium-doped propellants indicated ground state sodium distribution increases over the baseline.

The thesis is organized in the following sections. An overview of the basic theory of two-photon absorption laser-induced fluorescence and a set of rate equations including two-photon excitation, fluorescence, ionization, and amplified spontaneous emission is discussed. Following this, the details of the experimental setup are discussed, including a sodium-seeded gas-phase flame, sodium-doped propellant burning, and a microwave-coupled propellant burning experiment. The results of the gas-phase flame experiments are compared with the simple model and the results of sodium distributions in the propellant flames are discussed. Finally, in the concluding chapter, the prospects for quantitative measurements in the future application of the two-photon excitation scheme and a summary of the contributions of the thesis are presented.

CHAPTER 2. OVERVIEW OF DIAGNOSTIC MEASUREMENTS IN MULTIPHASE COMBUSTION

2.1 Introduction

In this chapter, an overview is given for optical techniques that have been applied to solid propellant flames, including emission spectroscopy, absorption spectroscopy, Raman spectroscopy and laser-induced fluorescence (LIF). In addition, the details of sodium LIF selection rules and a system of rate equations for the two-photon laser-induced fluorescence process are presented considering fluorescence, quenching, amplified spontaneous emission and ionization.

2.2 Overview of Optical Diagnostics for Multiphase Combustion Environments

Multiphase combustion environments are characterized by the presence of multiple coexisting phases. These environments consist of a complex interplay between gas-phase combustion, surface reactions, phase change processes, and a mix of diffusion and premixed combustion phenomena. Examples include solid propellant combustion for rocket motor applications, energetic material combustion, fires involving liquid fuel pools, and wildland fires. In these systems, the introduction of mechanical probes can significantly alter the local combustion phenomena through local heat transfer and reaction quenching effects, so the use of non-intrusive optical and laser diagnostics have often been employed. Compared to intrusive techniques such as a thermocouple or probe sampling, optical diagnostics have the advantage of making measurements with minimal disturbance to the flow field. In environments with particles and droplets and at high temperature, optical and laser-based techniques offer unique advantages in characterizing these combustion processes.

Non-intrusive optical methods have been used in a variety of gas phase combustion systems[14,25–27], but multiphase combustion environments present additional challenges[28]. The

efforts to characterize atomic sodium distribution presented in this dissertation are focused on applications in solid propellant flames, so the discussion will focus mainly on similar applications. Solid propellant flames present a particularly harsh environment because of multiphase, fast timescales (vaporization/volatilization/decomposition and kinetic), small scales of interest, and the presence of high temperature flames exhibiting both premixed and diffusion behavior. Also, the typical solid propellant flame structure is multi-zone, with significant variation in chemical composition. An example of the composite propellant flame structure is shown in Figure 2.1. As a solid propellant burns, both the oxidizer and the binder are preheated by conduction, resulting in a temperature gradient through the solid propellant[13,29]. The flame structure is typically composed of three distinct regions: partially-premixed flame, monopropellant flame, and a final diffusion flame. The diagram in Figure 2.1 shows the flame structure over a burning oxidizer crystal (ammonium perchlorate for the studies in this dissertation).

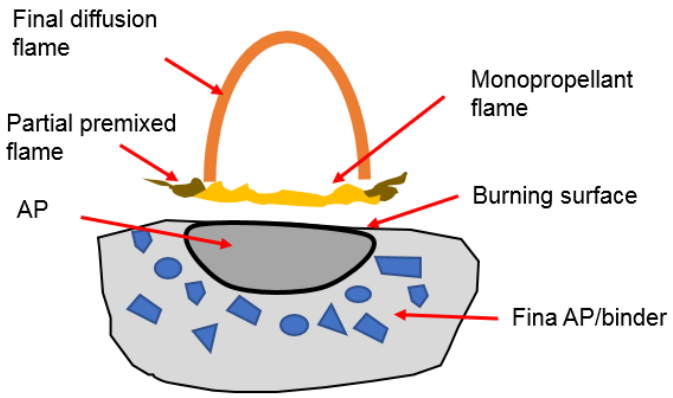

Figure 2.1 Composite propellant flame structure as illustrated by Beckstead et al.[29], and Hedman et al[30].

A number of optical and laser diagnostics have been employed to examine the complex reaction and flame structures on a variety of propellants.

This section presents the application of a variety of optical and laser diagnostics for measurement in solid propellant flames. These techniques include emission and absorption spectroscopy, Raman spectroscopy, and laser-induced fluorescence to target temperature and species concentrations.

2.2.1 Emission/Absorption Spectroscopy

Emission spectroscopy has been applied for identification of atomic and active intermediates in multiphase combustion. Spontaneous emission from upper states, excited either through the high temperature in the combustion region or through reactions resulting in electronically-excited fragments can be used to characterize typical hydrocarbon combustion intermediates (OH, CH) as well as particle combustion intermediates (aluminum monoxide, AlO[15]). For small molecules and atoms, these spectral features are well characterized, typically distinct from background emission, and can be used for estimates of species concentrations and temperature. Although making quantitative measurements of species concentration is complicated due to the path-integrated nature of the collection of emission, specific spectral peaks have been used to identify a variety of species present in flames.

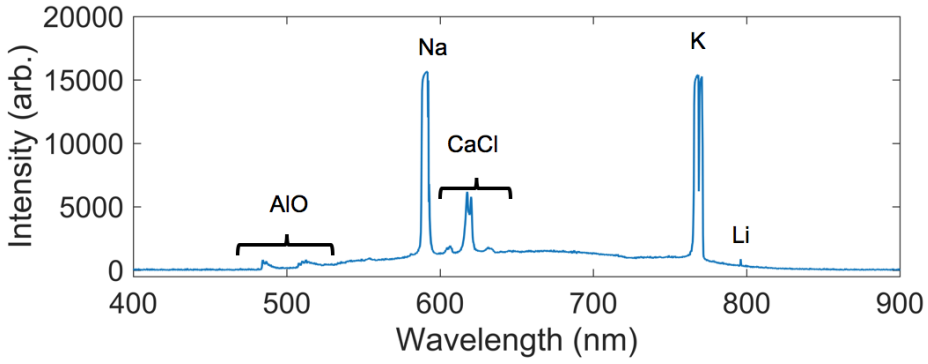

Figure 2.2 Emission spectrum of an aluminized propellant flame doped with 3.5% $NaNO_3$. Evident features include atomic emission peaks, combustion intermediates, and broadband blackbody emission.

Reaction products and intermediates in emission spectra can be identified through comparison with tabulated data on transition strengths and line positions through the National Institute of Standards and Technology (NIST) or similar databases[31]. A sample spectrum of an aluminized ammonium perchlorate/HTBP composite propellant is shown in Figure 2. This propellant contains 3.5% NaNO3 dopant, and there are spectral features associated with CaCl, K, Li, AlO, and Na and gray body emission. In addition, in other types of composite propellant emission spectra have also shown OH in the ultra-violet region[33], and H_2O, CO_2 and CO in the infrared region[32]. More studies using emission spectroscopy have been useful in characterizing species profiles[32], temperature[15,33], and combustion instabilities. In this thesis, emission spectroscopy is used as a global characterization of the propellant flame.

For multiphase combustion, the high temperatures and presence of condensed phases typically result in significant blackbody or gray body emission. The broadband emission has been used in propellant flames by characterization with two-color pyrometry[34]. By assuming the emission spectrum follows blackbody/gray body behavior, a temperature estimate can be made by using a Planck distribution and a known wavelength-dependent calibration for the collection system. For gas phase temperature measurements, the spectra of aluminum monoxide emission has also been used to indicate the temperature[33]. These temperature measurements have been used with good success, but can present bias as the gray body emission is biased towards the condensed phase and the AlO emission represents the temperature in the diffusion flame structure of aluminum droplet combustion.

While emission spectroscopy gives information tied to the upper state in a transition, absorption spectroscopy originates with the ground state and can be used to infer concentration, temperature, and pressure depending on the configuration utilized. Laser- and light-absorption

based methods are relatively simple to setup and have been used to identify species in solid propellant flames and in some instances to make quantitative measurements. The temperature and concentration of the molecule can be determined by fitting experimental spectra under some simple assumed experimental conditions.

Ultraviolet (UV) and visible (VIS) absorption is useful in avoiding strong blackbody interferences in multiphase flames, and transitions in this region typically correspond to low-lying electronic states. For small molecules and atoms, these transitions can be distinct and allow for species-selective excitation and detection. The UV/VIS range has been applied for absorption in solid propellant combustion processes to characterize important molecules and radicals including OH, NH, CH, HCN, H_2O, CO_2, CH_4, N_2O, and NO[32,35]. These small molecules are well-characterized in this spectral range and can be modeled for given temperatures, pressures, and concentrations. UV/VIS and IR absorption spectroscopy of research department explosive (RDX) combustion were employed by Vanderhoff[36] to understand molecules inside the dark zone-the region between the gas phase flame and burning surface where there is little emission of light. The experimental system consisted of a CO_2 laser for ignition, Xe lamp as an incident light source, and high-speed video was acquired simultaneously with the spectral acquisition system. Various species concentration such as OH, CN, NH and NO, and temperature were quantified for ambient pressures to 1 MPa using absorption spectroscopy.

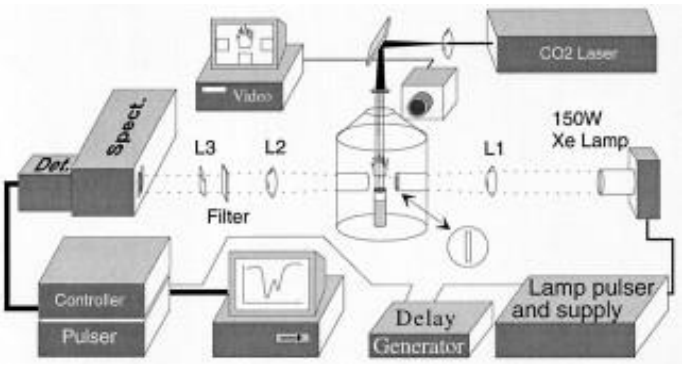

Figure 2.3 The optical experimental set up of absorption propellant experiments[36]. Reproduced with permission from Combustion and Flame.

Vanderhoff[36] extended these methods to infrared absorption experiments, as shown in Figure 2.3, to measure CO_2, H_2O, and HCN in the propellant product gases. These are all critical products and intermediates involved in the combustion chemistry. An absorption spectrum from Fourier Transform Infrared (FTIR) in the product region of RDX combustion is shown in Figure 2.4. Absolute species concentrations of CO, H_2O, HCN, CH_4 and N_2O, as well as rotational temperature, were extracted from the spectra[37].

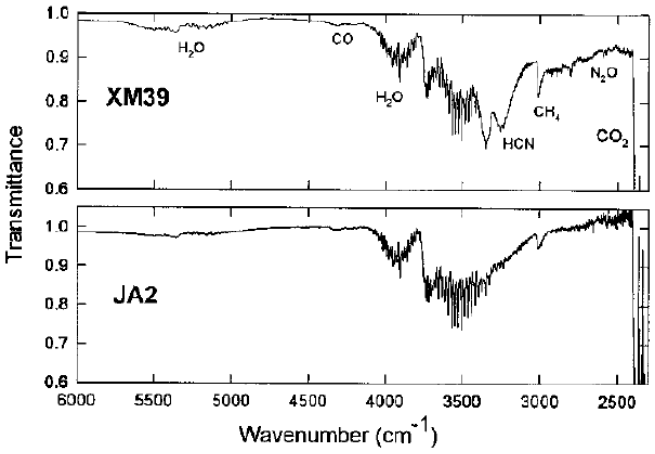

Figure 2.4 FTIR absorption spectrum in the IR range of both RDX-based XM39 and JA2. Species like HCN, N_2O, CH_4, CO_2, and H_2O have rotational-vibrational transitions that are observed using IR absorption spectrum[37]. Reproduced with permission from Combustion and Flame.

Absorption-based techniques can provide excellent quantitative information for multiple species, as demonstrated in RDX and propellant flame systems. However, particle scattering in multiphase combustion environments and strong background emission extending into the visible (gray body) can complicate the interpretation of laser-based absorption methods. In addition, absorption measurements are path-integrated, as are emission measurements. In highly variable, three-dimensional propellant flames, path-integrated techniques are challenging to apply for quantitative or localized information about the thermodynamic state or species concentrations. Many of these absorption techniques are limited by their temporal and spatial resolution when compared with other available methods.

2.2.2 Raman Spectroscopy

Raman spectroscopy is a widely used diagnostic for studying the rotational and vibrational structure of molecules. Rather than relying on path-integrated emission or absorption from rotational-vibrational-electronic transitions or rotational-vibrational transitions, Raman scattering techniques use inelastic scattering of incident light to infer rotational-vibrational information about the molecules. When the excitation laser beam interacts with an ensemble of molecules, inelastic scattering from the molecules can be generated which is shifted in energy by the difference between the ground and excited states. The inelastically-scattered photons then have energies corresponding to the vibrational and rotational states of the molecules. These techniques have been used extensively in combustion[38,39], but the focus here will be on applications in multiphase combustion. Parr and Hanson-Parr[40] built up a Raman scattering system shown in Figure 2.5, with a polarized Nd:YAG laser for illumination and a spectrometer to collect signal. The principal advantage of the Raman scattering technique is the detection of light in the visible to avoid interferences, and the potential for spatially-localized measurements. The range of molecules detectable via

Raman scattering includes symmetric molecules which are inaccessible via infrared absorption (N_2, O_2), and those with large dipole moments (HCl, H_2O) using a single laser source. However, the small scattering cross sections and low signal level presents an extreme challenge in the multiphase combustion environment where interferences can be significant.

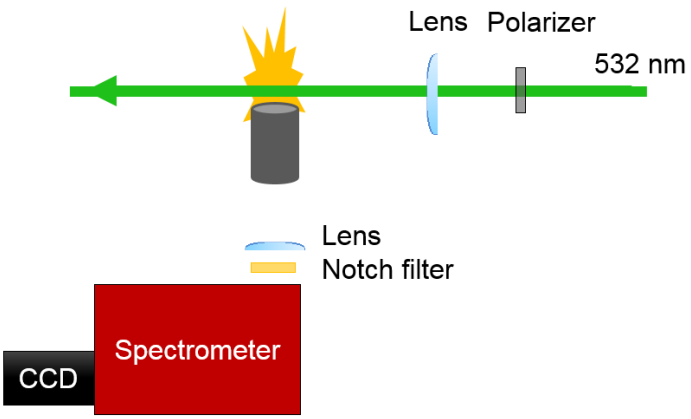

Figure 2.5 Raman Scattering experiments by Parr and Hanson-Parr to study nitramine-doped propellant flame[40].

Another application of Raman spectroscopy known as coherent anti-Stokes Raman scattering (CARS) has been used to examine solid propellant flames and multiphase combustion. The CARS technique involves multiphoton, nonlinear processes with targeted species such as N_2, H_2, and O_2[26]. The target molecule is pumped to a virtual state by tuning two lasers such that the difference between them matches a rotational or vibrational transition frequency. During this process (or shortly after). After Stokes shifting, a second pump beam (probe) interacts with the resonantly excited molecules and results in coherently-scattered photons. The CARS signal results from the near-simultaneous presence of these three fields and produces a laser-like signal[41]. CARS has distinct advantages over linear Raman scattering as previously described: the coherent process can result in a significant signal generation which

is easily detected due its laser-like propagation, and the focusing of the pump, probe, and Stokes beams can permit excellent spatial resolution (sub-mm). If pulsed lasers are utilized, the technique has high temporal and spatial resolution.

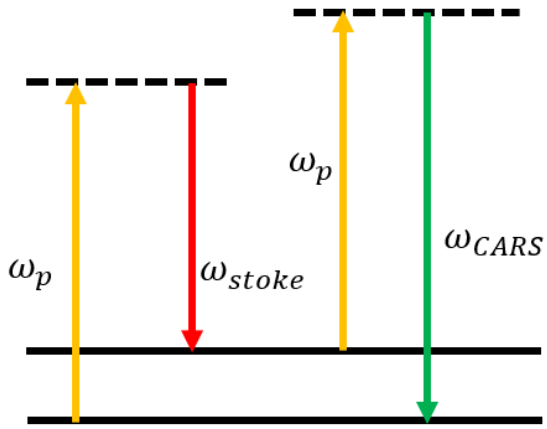

Figure 2.6 *Coherent anti-Stokes Raman scattering energy diagram. In typical configurations, the pump and probe are the same wavelength, while the Stokes beam is shifted relative to the pump beam to match a rotational or vibrational transition in the molecule of interest.*

The earliest CARS studies of propellant flames were conducted by Harris and Eckbreth[42,43]. Based on the fitting of the collected signal spectrum, species concentrations were calculated for H_2O, N_2, CO, and CO_2[44]. The flame temperature could also be inferred. Kearney et al.[45] introduced a hybrid femtosecond/picosecond CARS approach with improved detection by providing 'time-gated' elimination of strong non-resonant background interference through the time-delayed probe pulse. The results from an aluminized strand burn are shown in Figure 2.7 along with the experimental setup. Ultrafast or hybrid fs/ps CARS is a potential technique for probing the harsh, particle-laden, time-varying propellant combustion environment while eliminating strong interferences[46].

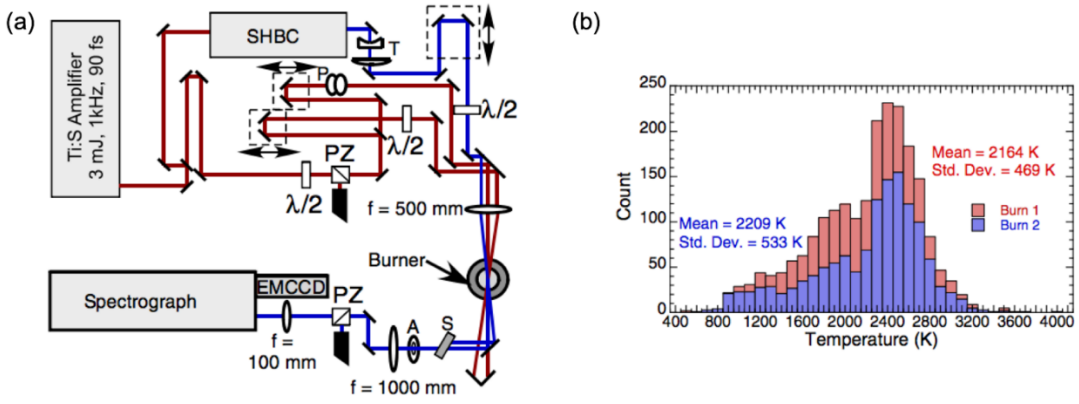

Figure 2.7 Ultrafast CARS system for propellant flame temperature measurements. (a) Schematic of fs/ps rotational CARS instrument; (b) Probability density function of nitrogen vibrational temperature showing fluctuations in the plume of the aluminized propellant strand burner. Reproduced with permission from U.S. Goverment.

2.2.3 Laser-Induced Fluorescence

Other laser-based techniques which can be applied in combustion environments include laser-induced fluorescence (LIF). Single-photon laser-induced fluorescence techniques were developed shortly after the introduction of the visible laser[14,24,47,48]. In laser-induced fluorescence, the laser wavelength is tuned to match a particular absorption line of the atom or molecule of interest. That species is excited to an upper electronic state, from which it fluoresces, and this fluorescence emission is detected. The spontaneously-emitted fluorescence signal intensity is related to the target atom/molecule concentration. Temperature can also be measured by determining the distribution of the molecules over rotational or vibrational levels. In gas-phase combustion, LIF has been applied extensively to measure species including but not limited to OH, CH, and NO[49,50], and resulting in significant databases for spectroscopy including quenching and energy transfer mechanisms.

Planar laser-induced fluorescence (PLIF)[14], a two-dimensional LIF technique, has been used extensively to study a variety of systems including laminar flames, turbulent flames,

combustion engines, and multiphase flows. PLIF involves forming the exciting laser into a uniform sheet of small thickness and significant height, and imaging the resulting fluorescent emission onto a sensitive detector array (typically an intensified charge-coupled device (CCD)). The principle advantage of PLIF is that regional variation in gas phase can be observed simultaneously. PLIF is also useful for transition events such as ignition and extinction. However, there are still multiple considerations in order to extract accurate, quantitative data. These include variations in quenching throughout the field, corrections for non-uniformity in the laser sheet, and laser energy corrections.

PLIF has also been widely applied to understand solid propellant combustion. Parr and Hanson-Parr[12,51,52] did pioneering investigations of propellant flame structure using PLIF of OH and CN radicals to help confirm phenomenological models for combustion of composite AP/HTPB propellants. In addition, they studied aluminum combustion in solid propellants using aluminum monoxide (AlO) PLIF, where the metal helped control combustion instability[51]. One challenge in applying PLIF to composite propellant flames and multiphase combustion systems is in the low repetition rate of traditionally available laser sources (10-50 Hz). Although each pulse corresponds to a time-resolved image, low repetition rates create challenges for data interpretation in highly time-varying propellant flames. This challenge can be addressed through the use of multi-kHz, high power laser systems consisting of either diode-pumped solid-state systems or burst-mode laser systems which have been used for combustion PLIF measurements at rates up to 100 kHz[53–56]. Hedman et al.[20,30] applied high-repetition-rate lasers (5 KHz) to make gas-phase OH PLIF measurements to understand bimodal AP/HTPB propellant ignition delay and diffusion flame structure at atmospheric and elevated pressures, as shown in Figure 2.8. They concluded that AP combustion behavior at 1 atm can be described

by a three-step process: protrusion above the surface as the surrounding binder burns away, ignition delay as the particle heats up, and regression as it deflagrates.

LIF measurements in flames can provide good molecular specificity and high detection limits (down to ppm levels). However, for several relevant combustion radical species, a single-photon detection is limited by the high photon energies required. For atomic O, H, N, single photon absorption (to the first electronically excited states) lies in vacuum ultraviolet range. These wavelengths that are difficult to generate and cannot penetrate through air or flame environments due to absorption by other major species (O_2, N_2, etc.)[57,58]. Moreover, for these atomic species using single photon excitation, the laser excitation and emission wavelengths may be identical and interferences are difficult to avoid. As a note, in LIF of OH, for example, the typical excitation schemes involve excitation to a state which fluoresces to a low-lying third state, rather than back to the ground state. For atomic species, interferences include signal trapping, strong attenuation of the incoming laser beam, re-fluorescence and the scattering of laser light which can not be rejected due to the identical excitation and emission wavelengths. Signal trapping refers to the absorption of emitted photons before reaching the detector and generally leads to a decrease in effective signal yield, which needs correction for quantitative measurements. In addition, re-fluorescence can lead to an effective elongation of the observed fluorescence lifetime and the broadening of flow features of interest. Alternative excitation and detection strategies have been explored previously using multiphoton laser excitation and subsequent fluorescence.

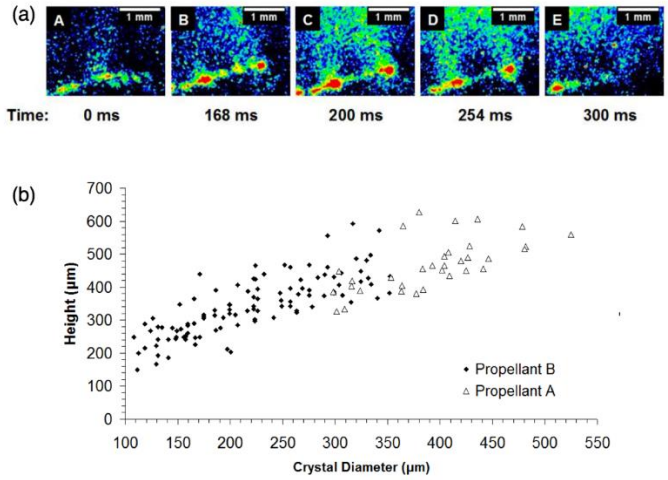

Figure 2.8 (a) Sequence of images showing the relative OH concentration above the burning surface. (b) Variation in height of the OH region directly above an AP crystal as a function of the crystal diameter. Reproduced with permission from Combustion and Flame.

Multiphoton techniques have been studied extensively in combustion environments using N atom, O atom, H atom, and CO where two-photon absorption allows the of accessible wavelengths[57–61]. For two-photon absorption, two photons are absorbed simultaneously through interaction with a virtual state and fluorescence is detected in another wavelength range. However, two-photon LIF has the issues of photon-ionization, photolysis in flames. Moreover, stimulated emission and saturation may also occur at high laser intensity. A lot of research has been done to avoid or reduce these issues to infer atoms concentration[62]. Goldsmith[58,63,64] reported photolytic interferences caused by H_2O and photodissociation could not be avoided of atomic hydrogen nanosecond two-photon LIF. Lucht[65] et al. have attempted to minimize the influence of quenching in two-photon LIF[66] measurement using a scheme called photoionization-controlled loss spectroscopy. Frank et al. have shown that picosecond laser is a promising alternative for O-atom two-photon LIF with dramatically reduced interference from CO_2 photolysis compared with nanosecond excitation. In addition, femtosecond two-photon laser-induced fluorescence could also avoid photolytic interference[67].

All of these issues make quantitative interpretation of two-photon LIF challenging to implement.

2.3 Microwave-Enhanced Solid Propellant Burning Rate

Plasma-assisted combustion is a promising technology to improve engine performance, increase lean burn flame stability[68], reduce pollutant emission[69] and assist low-temperature combustion[70]. A number of studies have employed microwaves for gas-phase combustion enhancement. Stockman et al.[71] demonstrated microwave enhancement for a field below breakdown threshold by increasing flame speed in a laminar, premixed CH_4/air wall stagnation flat flame. Moving to pulsed microwave systems, Michael et al.[72] demonstrated efficient coupling of microwave energy to flame by using high peak power pulsed microwave fields.

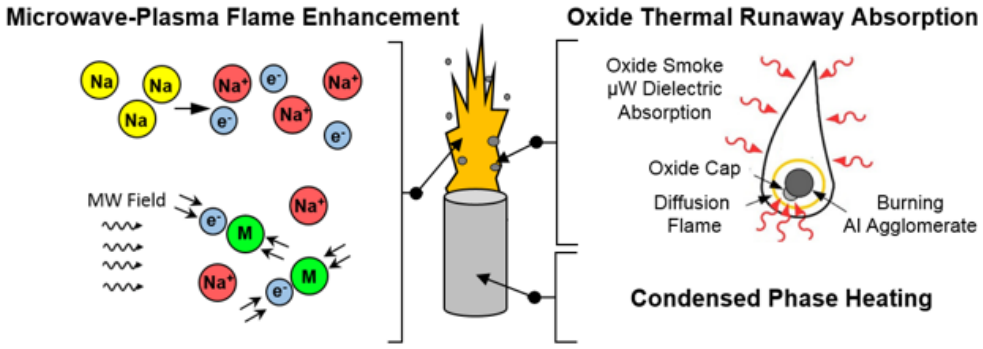

Figure 2.9 Illustration of proposed mechanisms for burning rate enhancement. Plasma kernel seeding occurs in regions of high local flame temperature (high free electron density) due to electron-neutral collisions and subsequently grows through the flame volume. Energy can be deposited through dielectric absorption to high temperature aluminum oxide features (oxide smoke and oxide cap) within aluminum droplet diffusion flames. Condensed phase heating can also contribute to the burning rate enhancement through dielectric absorption mechanisms.

In prior work, we have demonstrated the use of alkali metal doping for efficient, moderate-field-strength microwave energy deposition to the flame, which results in significant combustion enhancement[9]. The mechanisms of microwave energy deposition in alkali-doped solid propellant enhancement are highlighted in Figure 2.9, reproduced from Barkley et al[86].

Sodium can be easily ionized due to the high propellant flame temperature and low ionization threshold. In the investigations of microwave-enhanced propellant flame combustion, emission from sodium was observed with high-speed cameras and long-exposure spectrometers. To help determine the role of the sodium in promoting microwave energy absorption in propellant flame structure, more detailed information on the sodium distribution is required. Optical and laser-based techniques offer a promising method to infer ground-state sodium distribution with and without microwave field application with the goal of determining more precisely the mechanisms of burning-rate enhancement observed in these propellant flames with microwave illumination.

2.4 Review of Optical Techniques for Atomic Sodium

Optical techniques for measuring atomic sodium (Na) distributions have been investigated in a variety of combustion environments. Van Eyk et al.[21] developed a quantitative planar single-photon laser-induced fluorescence technique providing time-resolved measurements and planar distribution of atomic Na released from a single coal particle. However, the significant scattering from soot leads to low signal-to-noise ratio. Weiland et al.[74] applied one-photon excitation at 330 nm by detecting 818 nm to measure sodium concentration, where most of the photons relax by a resonant fluorescence emission. Hsu et al.[73] designed a novel application of laser-induced breakdown spectroscopy (LIBS) to provide quantitative measurements of Na from burning of brown coal and pine wood. However, the LIBS measurement is at point measure and a complex correction is needed for signal trapping. In single-photon LIF in multiphase combustion environments, particle scattering and signal trapping are the issues that are often limiting.

To avoid these problems, sodium two-photon LIF has been explored by Weiland et al.[74] and Allen et al.[75], as shown in Figure 2.10, for applications in optically dense combustors with

alkali salt seeding. Weiland et al.[74] reported two different two-photon excitation schemes: 3s-5s and 3s-4d. For both excitation schemes, they found the dependence of the two-photon LIF signal on laser fluence did not show the anticipated slope of 2 when plotting the signal versus laser fluence on log-log axes. This was attributed to ionization loss (detected for both transitions), amplified spontaneous emission (ASE), and quenching to other states. ASE and ionization during two-photon absorption laser-induced fluorescence process can become significant since the high sodium concentration in flame and ionization threshold is exceeded with a third low energy photon. Moreover, they reported the ASE signal as independent of laser power down to 2 mJ/cm^2, which was attributed to saturation of the excitation transition. They did not investigate excitation to the 3d state with a two-photon process. This process would have a direct fluorescent emission transition compared to the 3s-4d which they reported having relatively low quantum yield. Interestingly, they used a single-photon excitation of 3s-4p and found very strong emission from the 3d-3p transition[75].

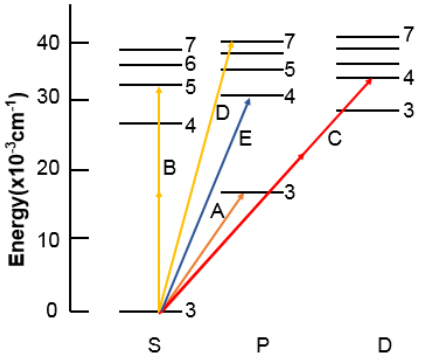

Fluorescence Transition	Excitation Transition			
	B (5s-3s)	*C (4d-3s)*	*D (7p-3s)*	*E (4p-3s)*
3p-3s	60			
4p-3s	0.07		0.07	75
5s-3p	2.4		0.03	
3d-3p	9.0	0.75	1.0	300
4d-3p	0.5	0.35	0.2	

Figure 2.10 Energy-level diagram for atomic sodium, illustrating the excitation schemes: A,3p resonance line; B, C, two-photon excitations; D, E, single-photon ultraviolet excitation at 260 nm and 330 nm; Table shows normalized fluorescence signal intensities from different excitation schemes.

This work explores single-photon excitation (3s-3p), two-photon excitation (3s-4d and 3s-3d), and subsequent fluorescence in environments which are highly scattering and of

significant sodium atomic density in gas phase flames and solid propellant flames. These environments are the highest number-density sodium systems examined in the context of combustion, and present significant challenges due to the multiphase combustion environment and the high number density of atomic species.

2.5 Theory and Rate Equation Modeling of Two-photon LIF

Two-photon excitation techniques allow access to additional transitions as the quantum mechanical selection rules allow changes of angular momentum $\Delta l = 0, \pm 2$ instead of the single photon selection rule of $\Delta l = \pm 1$. Three promising two-photon excitation schemes (3s-5s, 3s-3d, 3s-4d) and detection schemes (3d-3p and 3s-sp) are depicted on the energy level diagram shown in Figure 2.11. For these excitation schemes, the potential fluorescent detection photons are at 589nm, 818 nm, and 330 nm, as depicted in Figure 2.11. In considering the schemes for excitation, the experiments here utilized wavelengths easily accessible using the dye laser system (two-photon excitation at 578 nm, 602 nm, and 685 nm). For these, only two were examined in detail. The 3s-5s transition was investigated by Weiland et al., but not used here since the predominant signal generation was at 589 nm. In addition, the emission process is from a non-direct state and the potential for quantitative measurements would require detailed knowledge of the quenching and transition rate behavior leading to 589 nm emission. The 578 nm scheme is examined, but results in non-direct emission as well since the 4d-3p photon is outside of the easily detectable limit of the available imaging sensors. Finally, a new investigation of 3s-3d is carried out. Here the 3d state can emit a detectable photon directly.

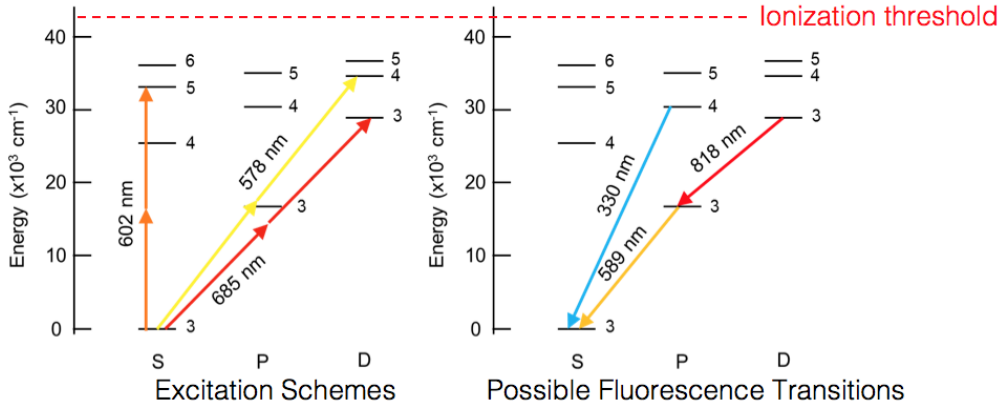

Figure 2.11 Sodium energy level diagrams depicting two-photon excitation strategies from the ground state (3s) are indicated in the left panel. Possible detection wavelengths which are directly or indirectly populated are indicated in the right panel.

In general, the smaller absorption cross-sections involved in multi-photon LIF techniques usually generate weaker signal than single-photon LIF techniques and therefore high power pulsed lasers are typically employed to increase the signal intensity level. However, the strong laser field generated by the lasers also results in additional nonlinear effects which complicate the interpretation of the signal. A good model is needed to help understand these nonlinear effects for multiphoton LIF techniques. A large amount of research has been done for the modeling of multiphoton processes to aid in the understanding of two-photon LIF, ionization, and ASE processes with the target of quantitative measurements for the targeted species. The measurements in this thesis provide data for validation of a sodium two-photon excitation fluorescence model taking into account these effects.

Rate equation models can be used to represent the atomic system under consideration, as previously described by Amorim[76,77] for atomic oxygen. For the atomic sodium system under consideration, a four-level system should be considered with the four states corresponding to the 3s (N_1), 3p (N_2), 3d (N_3), and ionized (N_i) levels. In general, this system can be used for any atomic system. It involves a four-level system interacting with a laser

pulse. The laser pulse excites the target atom from the ground state (N_1) to the excited level (N_3) via two-photon absorption. Atoms in the excited state can either absorb another photon to be ionized, spontaneously emit a photon to proceed back to the intermediate state (N_2) or undergo quenching. Due to the two-photon excitation and high-lying excited state, amplified spontaneous emission is almost always prevalent in two-photon excitation systems. This has been examined for O atom, H atom, and N atom in both combustion and plasma systems[57-61]. The amplification of a stimulated emission wave can be considered for a given laser focusing geometry. Models exist in the literature for zero-dimensional, one-dimensional, and two-dimensional geometries based on rate equation and Monte Carlo approaches. In this chapter, the rate equations are detailed that should be incorporated into such an analysis. Amorim et al. implemented a 1D numerical model for atomic oxygen and compared to experimental data[78]. The O atom model is implemented using a hyperbolic partial differential equation solver[79] and the rate equation system is presented as the following:

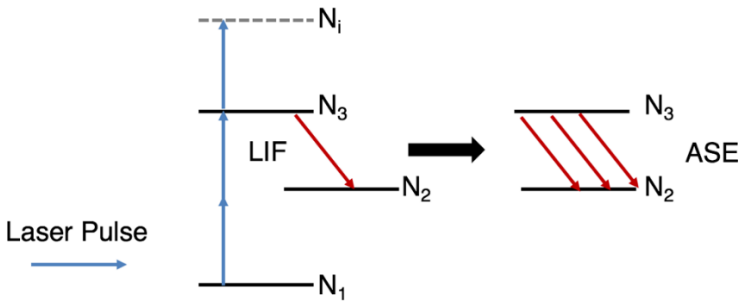

Figure 2.12 Illustration of two-photon LIF process.

$$\frac{dN_1}{dt} = -\left(N_1 - \frac{g_1}{g_3}N_3\right)\frac{\alpha_{1,3}\phi_l^2}{h\nu_l} + N_2(A_{2,1} + Q_{2,1}) + N_3 Q_{3,1} \quad (1)$$

$$\frac{dN_2}{dt} = N_3(A_{3,2} + Q_{3,2}) - N_2(A_{2,1} + Q_{2,1}) + \frac{B_{3,2}I_{se}}{c\Delta\nu_{se}}\Gamma\left(N_3 - \frac{g_3}{g_2}N_2\right) \quad (2)$$

$$\frac{dN_3}{dt} = \left(N_1 - \frac{g_1}{g_3}N_3\right)\frac{\alpha_{1,3}\phi_1^2}{h\nu_l} - N_3\left(\frac{\sigma_{3,i}\phi_l}{h\nu_l} + Q_{3,2} + Q_{3,1} + A_{3,2}\right) - \frac{B_{3,2}I_{se}}{c\Delta\nu_{se}}\Gamma\left(N_3 - \frac{g_3}{g_2}N_2\right) \quad (3)$$

$$\frac{dN_i}{dt} = N_3 \frac{\sigma_{3,i}\phi_l}{h\upsilon_l} \quad (4)$$

$$N^{LIF} = N_3 A_{2,1} \quad (4)$$

For this system of equations, the following parameters are used:

c and h: the speed of light and the Planck constant;

ϕ_l: the radiance of the excitation laser pulse;

υ_l and υ: the frequency of the pump laser and fluorescence;

$\alpha_{1,3}$ and $\sigma_{3,i}$: the two-photon absorption cross section and photon ionization cross sections;

$g_i (i = 1, 2, 3)$: the degeneracy of each level;

A: the Einstein A coefficients;

Q: the collisional quenching rates of different states;

$\Delta\upsilon_{se}$: the linewidth of the ASE radiation, in this work, $\Delta\upsilon_{se} = 1\ cm^{-1}$. In this system, gain narrowing and broadening of ASE radiation linewidth was not considered.

Γ is the overlap integral defined as $\Gamma = \int g(\upsilon) \times f(\upsilon) d\upsilon$ with $g(\upsilon)$ and $f(\upsilon)$ representing the line shape function of the absorption transition and the ASE radiation. In this work, $g(\upsilon)$ and $f(\upsilon)$ were assumed to be Gaussian profile with the same linewidth, resulting in a constant $\Gamma = 0.5$. $B_{3,2}$ is calculated through $B_{3,2} = A_{3,2} c^3 / 8\pi h\upsilon^3$

In order to take account of the ASE propagation, both one-dimensional and two-dimensional (Monte Carlo) simulations have included photon transport equations in the forward and backward directions which were solved simultaneously with the rate equations in each specific slices, considering the flux of photons from adjacent segments.

$$\frac{dI_{se,f}}{dx} = \left(\frac{B_{3,2}I_{se,f}}{c\Delta v_{se}}\Gamma\left(N_3 - \frac{g_3}{g_2}N_2\right) + N_3A_{3,2}\frac{\Delta\Omega_f}{4\pi}\right)h\nu \quad (5)$$

$$\frac{dI_{se,b}}{dx} = \left(\frac{B_{3,2}I_{se,b}}{c\Delta v_{se}}\Gamma\left(N_3 - \frac{g_3}{g_2}N_2\right) + N_3A_{3,2}\frac{\Delta\Omega_b}{4\pi}\right)h\nu \quad (6)$$

$$I_{se} = I_{se,f} + I_{se,b} \quad (7)$$

The solid angle formed, H , T, and L are the height, thickness and length of the simulation domain.

$$\Delta\Omega_f = 4\tan^{-1}\left(\frac{T}{2(L-x)}\right)\sin\left(\tan^{-1}\left(\frac{H}{2(L-x)}\right)\right) \quad (8)$$

$$\Delta\Omega_b = 4\tan^{-1}\left(\frac{T}{2x}\right)\sin\left(\tan^{-1}\left(\frac{H}{2x}\right)\right) \quad (9)$$

This model is only proposed in this thesis. But the goal is to compare the model and experimental data on fluence dependence of fluorescence, ASE, and ionization was collected. One final point is the potential need for an extension of this type of modeling for sodium. In O atom, where this was previously applied, the excited states are few and of high energy, so a 3-level system was adequate. In sodium, because of the lower energies of the excited states, it may be necessary to model additional energy transfer processes. In particular, for plasma systems, energetic collisions may be sufficient to generate significant excited state populations of sodium atoms which may impact the assumptions of using a three-level system.

CHAPTER 3. EXPERIMENTAL SETUP

3.1 Setup Overview

Due to the harsh environment present in propellant flames, laser-based combustion diagnostics have potential as non-intrusive, in-situ, and high resolution (temporal and spatial) measurement techniques. In this thesis, laser-induced fluorescence is applied to understand ground-state sodium distribution in microwave assisted, sodium-doped propellant flames. Experiments on sodium fluorescence were conducted in a sodium-seeded gas phase flame and in sodium-seeded composite propellant flames. The fluorescence excitation and detection schemes investigated are discussed and the premixed flame burner used for characterization is introduced. Details of one-photon and two-photon laser-induced fluorescence systems in a flame are given.

The final two sections detail the propellant formulations and microwave systems used throughout the experiments. For solid propellants, the formulations and equilibrium calculations of sodium concentration and flame temperature are presented to estimate equilibrium sodium atomic concentrations. Finally, the apparatus used to deposit continuous-wave microwave energy to the flame structure doped with alkali metal is presented, along with a description of the timing and simultaneous collection of atomic emission.

3.2 Diffusion and Premixed Flame Burner

For fluorescence characterization, a non-premixed diffusion flame and a premixed flat flame were used as shown in Figure 3.1. The non-premixed diffusion flame consisted of a 2-inch outer co-flow with velocity-matched air and a 0.5-inch inner tube flowing 0.2 SLPM of natural gas with sodium seeding. The premixed flat flame burner followed the design of Hartung et al[80]. with slight modifications to the burner surface due to fabrication limitations.

All burner parts were fabricated from brass, except a copper cooling loop which was brazed to the outer burner surface. The top plate consisted of a brass plate with 0.8 mm holes with an open area of ~35 percent. A dimensioned drawing of the burner plate and assembly are shown in Figure 3.2. The modified diameter is still much smaller than the minimum quenching diameter for a CH_4/air flame, and the steel wool in the original design was replaced with 2 mm glass beads to avoid corrosion by the seeded solvent.

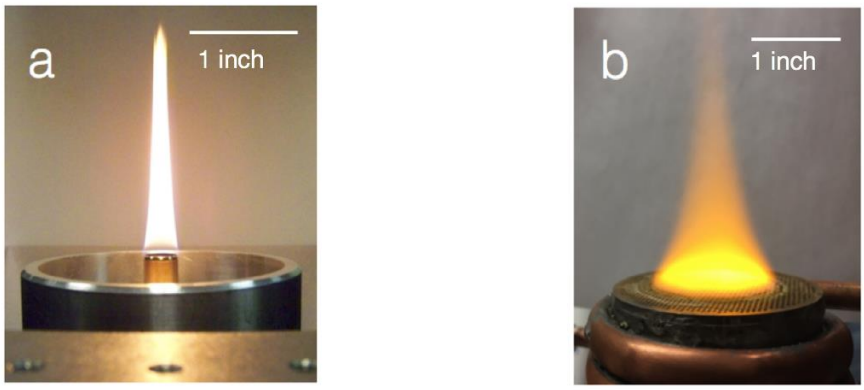

Figure 3.1 (a) *Non-premixed diffusion flame with an air co-flow; and (b) Premixed flat flame burner with sodium-seeding in the central flow via atomized methanol/$NaNO_3$ solution.*

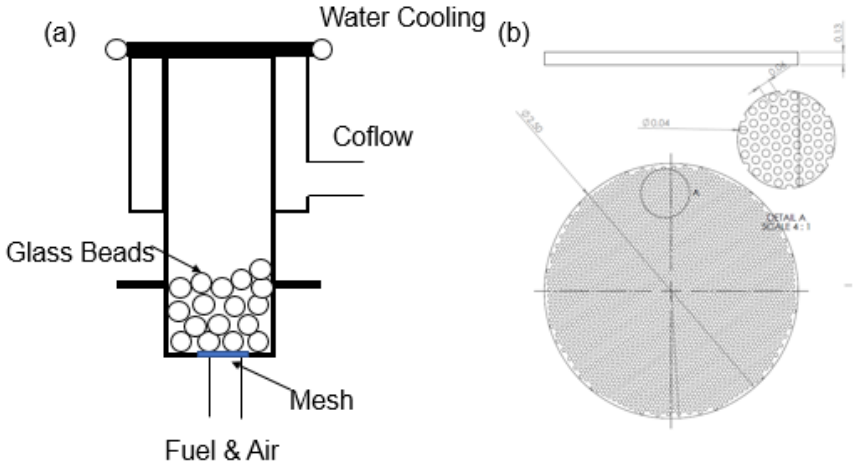

Figure 3.2 Premixed flat-flame burner. (a) body design, (b) modified top plate design

The premixed flame was run over only the central portion of the burner with 1 standard liters per minute (SLPM) of natural gas and 3 SLPM of air. Sodium was seeded into the flames using a droplet seeder (TSI Aerosol Generator 3760) using a sodium chloride in water or sodium nitrate in methanol solution at three different concentrations. Flow rates for the gas were metered with Alicat mass flow controllers with an accuracy of 1%, with the calibration of MesaLabs Defender 530+, and the volume flow rate of the aerosol seeder was measured by Cole-Parmer flow meter. To match the propellant formulation, sodium nitrite was seeded into gas-phase flame. The estimated sodium concentrations are listed in Table 3.1 based on the metered flowrates used as inputs to the NASA Chemical Equilibrium with Applications (CEA) solver.

Table 3.1 *Flow rate of gases and predicted sodium concentration in flame.*

Burner	**Natural Gas (SLPM)**	**Air (SLPM)**	**Solvent/$NaNO_3$ concentration (g/L)**	**Predicted equilibrium Na concentration (ppm)**
Diffusion	**0.2**	**3.2**	**Methanol, 1 g/L**	**500**
Premixed	**0.5**	**5.6**	**Methanol, 10 g/L**	**4000**
Premixed	**1**	**5**	**Water, 25 g/L**	**6000**

3.3 Laser-induced Fluorescence System

Laser-induced fluorescence has been a prominent laser diagnostic tool for targeting combustion-relevant species and products since the advent of the pulsed laser. In LIF, the frequency of a laser beam is tuned to a specific electronic transition of an atom or molecule. The targeted species is excited by absorption of a laser photon to a higher energy state. The excited-state photons decay back to the ground state by radiative (spontaneous emission) or nonradiative decay. This spontaneous emission process is classified fluorescence, and the

signal is typically detected by photosensitive elements. Concentrations and temperatures can be determined based on the LIF signals. Planar laser-induced fluorescence is the two-dimensional variant of this technique.

Sodium LIF has been investigated in a variety of combustion and aerodynamic environments due to the easy accessibility of the sodium D line transition and its extremely high absorption cross section. Although sodium one-photon LIF has been successfully used to measure the velocity[88], temperature[89], and concentration[21] of seeded gaseous jets, they often require corrections in high optical density environments due to the resonant excitation and collection of the fluorescence signal. As discussed in Chapter 2 for the one-photon absorption LIF in sodium, the easiest transition to access (D-line) has a resonant detection wavelength which is the same as the excitation wavelength. For atomic systems with high density, this leads to the re-absorption and re-fluorescence of LIF photons before reaching the edge of the flame and the detector. The first sub-section will describe some initial characterization with the one-photon LIF system.

The high optical density caused by the sodium concentration and the inability to distinguish between the wavelength of laser scattering from particles and the fluorescence signal in the solid propellant flames made one-photon LIF too difficult to apply. Two alternative methods of using two-photon absorption LIF with emission at different wavelengths will be explored in this thesis. These multiphoton processes are also subject to amplified spontaneous emission (ASE) and ionization losses that can complicate interpretation of the signal. The second section of this part will discuss details of two-photon LIF experiments setup to understand the relationship between fluorescence, ionization, and ASE.

3.3.1 Single-photon Excitation LIF

The nanosecond LIF system is shown in Figure 3.3. A 10 Hz Spectra-Physics Quanta-Ray Nd:YAG laser, ~200 mJ/pulse at 532 nm, was used to pump a Continuum ND 6000 dye laser with Exciton Rhodamine 610 for the 3s-3p excitation of sodium (589 nm) at approximately 40 mJ/pulse. A portion of the dye laser output (10%) was used to monitor wavelength with a Highfinesse Wavemeter WS-6. The remainder of the beam (90%) was focused into the flame. A +125 mm focal length lens was used to focus the laser beam, and a +400 mm plano-convex cylindrical lens was also used to generate a sheet with a thickness of 1.4 mm (10/90 width) and 10 mm height. A fast-gated intensified-CCD camera (Princeton Instruments, PI-MAX 2) with a 55 mm, f/1.2 Nikon objective lens was set orthogonal to the laser sheet to collect the fluorescence signals. A 590 nm bandpass filter (Asahi Spectra, ZBPA590, FWHM: 11 nm) was used to detect 589 nm fluorescence emission. A digital delay generator (Stanford Research Systems, DG-535) was used to synchronize the laser and camera systems.

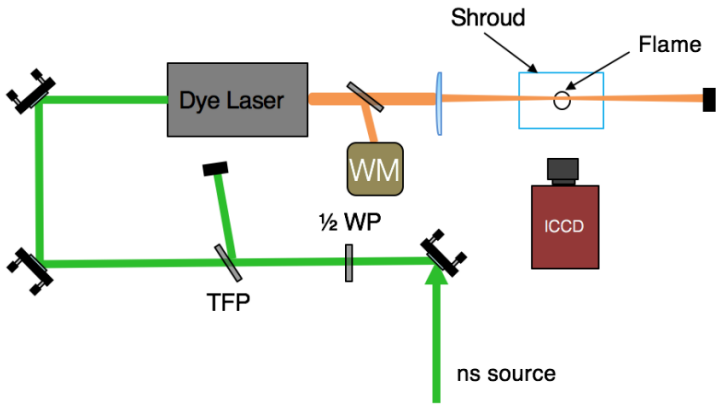

Figure 3.3 *Schematic of experimental setup for nanosecond pulsed laser one-photon laser-induced fluorescence showing the dye laser pumped by the second harmonic of Nd:YAG laser, the flame and shroud, sheet-forming optics, and the ICCD. Symbols indicate the following: SHG-second harmonic generation; WM-wavemeter; TFP-thin film polarizer; ICCD-intensified CCD; WP-wave-plate.*

3.3.2 Two-photon Excitation LIF

Two-photon laser-induced fluorescence has the advantage of avoiding fluorescence trapping or re-emission as compared to single-photon excitation. As discussed in Chapter 2, Weiland et al. reported strong ionization signals based on nanosecond two-photon excitation transitions of optically dense sodium-doped flame. Three promising excitations and fluorescence detection were laid out in Chapter 2. In this thesis, 3s-4d excitation (578 nm) will be investigated, but non-direct excitation of the original states of the observed 589 nm and 818 nm emission complicate the analysis of fluence dependence without a kinetic model including collisional activation and deactivation of the relevant states. The 3s-3d (685 nm) two-photon excitation, which has a direct fluorescence emission 3d-3p (818 nm) will be presented, which Weiland et al.[61] did not report. The laser system is the same as for one-photon experiments (Nd:YAG-pumped dye laser) with a change to a different Rhodamine 610/640 mixture for two-photon 3s-4d excitation at 578 nm, and Rhodamine 640 for 3s-3d two-photon excitation at 685 nm. A summary of the dye mixtures and performance for the three excitation wavelengths is given in Table 3.2. For the detection of 818 nm fluorescence imaging, a 1-inch 820 nm bandpass filter (Thorlabs, FB820-10) was placed before the objective lens. Both sodium-doped premixed flames and sodium-doped propellant flames were investigated by two-photon PLIF, with results presented in Chapter 4.

Table 3.2 Dye mixture for the three wavelengths excitation wavelength of atomic sodium LIF.

Excitation	Dye	Concentration (mg/mL) Osc and Amp
3s-3p (589 nm)	**Exciton Rhodamine 610**	**120.6 and 51**
3s-4d (578 nm)	**Exciton Rhodamine 610/640 mixture**	**21.3/37.8 and 10.6/18.7**
3s-3d (685 nm)	**Exciton LDS 698**	**75.6 and 18.9**

For two-photon excitation, a significant degree of ionization and amplified spontaneous emission are expected due to the high sodium levels present in these flames and the low ionization threshold for sodium. Weiland et al.[61] reported data on these, but it is necessary to replicate these results for the range of interest in sodium-doped propellant flames and for the additional two-photon scheme that we investigate for the first time. The setup for measurement of correlation between ASE, ionization, and fluorescence of two-photon 685 nm excitation is detailed in Figure 3.4. The dye laser energy is controlled by a polarizer and a plano-convex spherical f=+200 mm lens was used to focus the laser beam 10 mm above the burner surface. A portion of laser pulse was picked off with a thin glass slide and sent to the photodiode to record the laser energy fluctuations. The integrated photodiode signal through the boxcar was calibrated against a power meter. A photomultiplier tube (PMT, Hamamatsu, H10722-20) with a high voltage supply was used for detection of the fluorescence emission with collection by a +60mm plano-convex spherical lens. An 820 nm ultra-narrow filter (Alluxa 820-2006) and RG780 long pass filter were placed before the PMT. To collect ASE signal from the burner, a dichroic mirror (Semrock, FF801-Di02) was used to pass the excitation laser and reflect the 818nm ASE. The reflected ASE beam (with focusing parameters close to that of the pumping beam) was collected onto a photodiode (Thorlabs, DET36A) with an 820 nm bandpass filter (Thorlabs, FWHM 10 nm) using a +150 mm plano-convex spherical lens. An ionization probe was constructed similar in design to that developed by Cool et al. to detect laser-generated ionization. The probe was set ~ 2 mm from the laser focus in the premixed flat flame. Single-shot signals from the photodetectors for ASE, laser energy, fluorescence, and the ionization were collected for a range of laser energies using a Stanford Research Systems 250 Boxcar Integrator and sent to an NI DAQ (BNC2110) board to be recorded by a National Instruments

data acquisition system (DAQ). The boxcar was triggered at 10 Hz, and consists of gated analog integration. The DAQ board was used to read the DC signal level corresponding to each channel at the laser repetition rate of 10 Hz (See Appendix A).

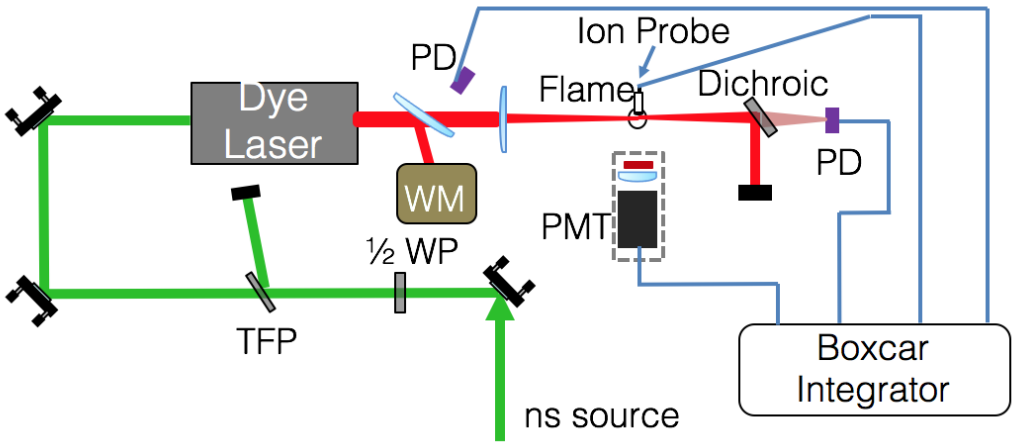

Figure 3.4 *Schematic of experiment showing two-photon excitation experiment to monitor shot-to-shot variation in laser energy, fluorescence by PMT, ASE and ionization with a Boxcar Integrator*

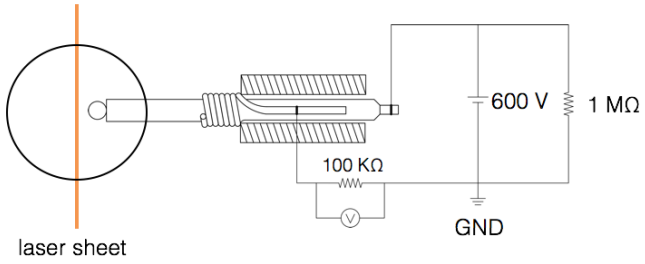

Figure 3.5 *Ionization detection probe adapted from Cool et al*[90].

A schematic of the ionization detection probe is shown in Figure 3.5. The probe consists of an anode of a 0.8 mm diameter spherical bead of platinum on the end of a piece of 0.4 mm diameter platinum wire. A ceramic insulator is used to shield the anode except for the bead end, and the cathode consists of another platinum wire coiled around the insulator and enclosed by another piece of insulator. The signal was detected with a Tektronix MDO3054

oscilloscope and a 100x attenuating voltage probe (Tektronix P6139B, 10MΩ). Acquisitions were typically AC coupled to minimize the contribution from the flame ionization signal (a constant voltage offset). For the boxcar measurement, a 1 kHz high pass filter (100 nF and 1.5 kΩ) was used to replace the voltage probe.

3.4 Propellant Formulation

A range of composite propellant formulations varying the amount of aluminum, ammonium perchlorate (AP) and Sodium nitrate ($NaNO_3$) dopant were used for combustion experiments. The propellant formulation, shown in Table 1, consisted of aluminum (~ 35 µ*m*, Valimet-H30), bimodal AP (200/90 µ*m*, 80/20 wt.% Firefox Chemicals), $NaNO_3$ (Firefox Chemicals), and hydroxyl-terminated polybutadiene (HTPB). Details on propellant manufacturing process are given by Barkley et al[9]. In short, $NaNO_3$ was milled first and mixed with binder/AP at room temperature for three hours. And strands were cured for seven days at 60 °C. Propellant adiabatic flame temperatures were simulated in Cheetah[81] equilibrium solver as reported in Table 3.3.

Table 3.3 *Propellant formulations*

	Propellant Compositions				
Formulation Name	**NaNO3 (<75 µ*m*)**	**AP (200/90 µ*m*)**	**Al (35 µ*m*)**	**HTPB**	**$T_{flame, ad}$ (1 atm), (K)**
Al-AP-NaNO3 3.5%	**3.5**	**70.5**	**14.5**	**11.5**	**3037**
Al-AP-NaNO3 1.0%	**1.0**	**72.6**	**14.5**	**11.9**	**3029**
AP-NaNO3 3.5%	**3.5**	**84.9**	**0**	**11.6**	**2711**
AP-NaNO3 1%	**1.0**	**87.1**	**0**	**11.9**	**2717**

Single-photon and two-photon excitation of Na were applied to sodium-doped propellants without microwave coupled condition. The diagnostic system is consistent with Figure 3.3 (Single photon one). Instead of a flat flame burner, a ~3 cm height propellant strand was set in a transparent box and a vent was used to ventilate the product gases. For these studies, the ICCD camera was used with zero gain.

3.5 PLIF in Microwave Systems

The main test apparatus for microwave-assisted solid propellant burning experiments consisted of a basic microwave system and laser setup as just described. In addition to the fluorescence imaging, a high-speed camera was synchronized to take the images to indicate the burning rate, sodium emission, and particle emission. Data from the microwave system was acquired with an oscilloscope.

3.5.1 Microwave System

The configuration of the rectangular microwave resonant cavity assisted solid propellant burning is similar to that used by Stockman et al[71]. It has the advantage of single mode operation, the ability to impedance match to the load, high cavity quality, and optical access for laser introduction and imaging. The core components of the experimental apparatus consist of the magnetron, waveguide sections, and test section. An 870 W, 2.46 GHz continuous wave (CW) magnetron (National 2M107-825) launched into a WR284 waveguide cavity and propagated in a TE10 mode through a waveguide transition to connect with a WR430-scale test section (modified cavity design in appendix B). The forward and reflected power were measured with a Schottky diode (Pasternack PE8003) and signals were recorded on an oscilloscope (Tektronix MSO 70404C).

The test section consisted of a custom WR430 cross section waveguide test section. The test section had optical access for the laser beam to cross at orthogonal angles to two

oppositely set viewing windows. In order to minimize the loss and leakage of the microwave, aluminum wireframe grids were set in the cavity walls with a small opening (5 mm). This size is insufficient to attenuate the microwave and avoid any propagating microwave mode. To prevent exposure of microwave components to corrosive propellant combustion exhaust, the test section is modified by insertion of two 19.81 mm thickness polytetrafluoroethylene (PTFE) blocks as purple in Figure 3.6. Within the test section, propellant strands were ignited by a two-second duration, 2-watt blue diode laser from the top. Smoke, generated by solid propellant burning, was evacuated from the cavity by an air co-flow produced by cyclone vacuum application.

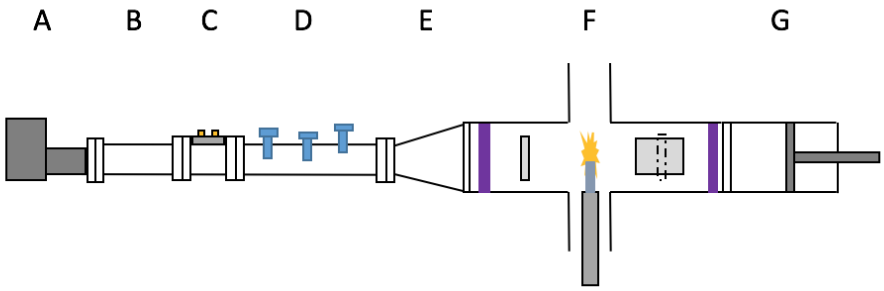

Figure 3.6 Microwave waveguide resonator. The microwave system consists of (A) a magnetron launching into WR284 waveguide, (B) a circulator, (C) directional coupler with Schottky diodes, (D) a stub tuner, (E) a WR284 to WR430 transition section, (F) test section for propellant burning with polytetrafluoroethylene (PTFE), (G) a sliding short section. The colored blocks in the test section (F) indicate the place of Teflon blocks to prevent corrosive products from reaching the sensitive components of the cavity.

The cavity was impedance matched to a half-length propellant strand (~1cm) by stub tuning and achieve a high quality factor (Q-factor). COMSOL Multiphysics 5.0 was used to simulate the unloaded cavity and help select position of the sliding short distance. A numerical simulation of electric field strength within the test section with PTFE, as shown in Figure 3.7,

with an input port (TE10 mode, 1 kW input power).. For a microwave resonator, field energy is stored and this is typically quantified by determining the quality of the cavity. This is defined as the frequency multiplied by the ratio of the field energy stored in the cavity over power loss rate from the cavity. The theoretical quantification of resonance for a microwave cavity is the defined as:

$$Q = \omega \frac{W}{P_{loss}} = \frac{\omega}{\Delta\omega_{3dB}}$$

where ω is the angular frequency of the microwave radiation, W is the energy stored within the cavity, and P_{loss} is a measure of the energy lost to the load and ohmic heating of the walls. The right-hand side of the equation provides an experimentally obtained parameter from the VNA to calculate Q, where $\Delta\omega_{3dB}$ is the 3 dB width of the cavity resonance at the microwave frequency. To measure the Q-factor of the unloaded microwave, a vector network analyzer (VNA, Anritsu MS46322A Shockline) with APC-7 calibration kit was used to determine a Q of ~90.

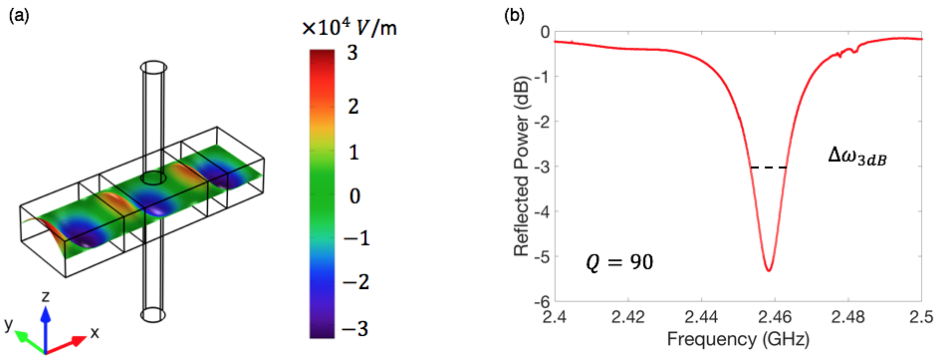

Figure 3.7 *(a) Microwave E-field strength simulation results using COMSOL; (b) Resonant wavelength Quality-factor measurements of WR 430 cavity using a Vector Network Analyzer.*

3.5.2 PLIF Diagnostics

The wavelength for two-photon excitation of the 3s-3d transition of sodium (685 nm) was generated as described in section 3.3.2. A combination of a -300 mm cylindrical lens and a + 200 mm plano-convex spherical lens was used to generate a laser sheet to go through the slot of the microwave test section as in Figure 3.8 (a). Due to the cavity design, the camera cannot be set orthogonally to the laser sheet to collect fluorescence intensity.

In order to take the emission and fluorescence images simultaneously, a 2-inch Pellicle beamsplitter (Thorlabs, R/T = 45/55) was used as shown in Figure 3.8 (a). The transmission (fluorescence) was detected by a Princeton ICCD fast-gated camera (gain at 100) at 5 Hz and the reflection was collected by a Photron SA-X2 high-speed camera at 1 kHz or by backlit imaging using Chameleon CCD camera (FLIR/PointGrey) at 10 Hz. For the detection of 818 nm fluorescence images, an 820 nm ultra-narrow bandpass filter (Alluxa) and RG780 long pass filter (Thorlabs) were placed before the 105 nm Nikon lens and 96 mm extension tubes. For the detection of emission imaging, a 589 nm bandpass filter and an RG610 long pass filter (Thorlabs) were placed before a 105 mm Nikon lens with 84 mm extension tubes.

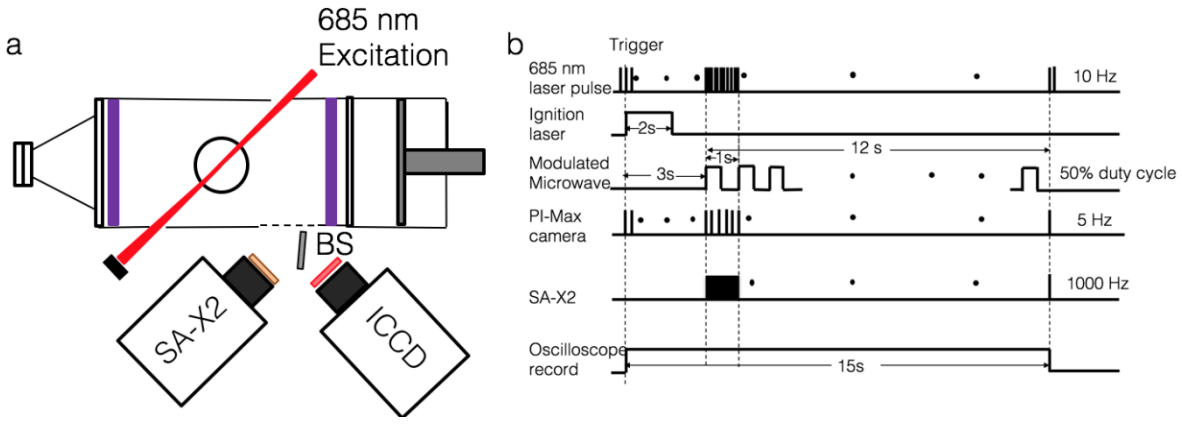

Figure 3.8 *(a) Sodium two-photon PLIF setup with the microwave test sections simultaneous high-speed imaging of sodium emission. (b) A timing diagram showing the synchronization and modulation of the microwave field.*

To time and synchronize the experiment, a digital delay generator (Berkeley Nucleonics Corporation, Model 575) was externally triggered by a master clock (Stanford Research System DG535), which was running the Nd:YAG laser Q-switch. A copy of the trigger to the PI camera was used to trigger a second delay generator (BNC Model 577), which is used to synchronize the high-speed camera, trigger ignition, and modulated microwave. The full sequence is depicted in Figure 3.8 (b), where a total sequence spans 15 seconds. Initially, a 2W blue diode laser was activated for 2s to ignite the propellant strands. After one additional second (allowing for steady burning), the high-speed camera and microwave were activated, and the microwave was modulated at 1 Hz and different duty cycles in experiments. The forward and backward-directed microwave power in the cavity were monitored via Schottky diodes (Pasternack PE8003) on a Tektronix MSO70404C oscilloscope. The diodes were calibrated using a power meter (Keylight, N1912A, P-series).

A series of experiments were conducted varying the composition and comparing the case of no applied field and applied field, with the goal of determining the role of the atomic sodium distribution in the propellant burning rate enhancement with the application of high strength microwave fields. Burning rate enhancements were measured for each strand, and backlit imaging allows for better comparison with the Na fluorescence images. Sodium fluorescence images were taken for a range of microwave field duty cycle and propellant compositions, as laid out in Table 3.3.

CHAPTER 4. RESULTS AND DISCUSSION

This chapter describes a series of experimental results of one-photon and two-photon laser-induced fluorescence in sodium-doped flames. Despite the potentially straightforward analysis of single-photon excitation, there are several drawbacks: the detection and excitation wavelengths are resonant, and fluorescence trapping is expected to be significant in high sodium number density flame environments. As an alternative, two-photon excitation schemes are examined to avoid significant fluorescence trapping and to allow time-gated and optically filtered detection away from the excitation wavelength. Results from two schemes (3s-4d and 3s-3d) of two-photon excitation fluorescence will be shown in this section. In addition, single-photon and two-photon excitation were applied to propellant with and without microwave application to analyze the ground state sodium distribution in the harsh environmental conditions.

4.1 Laser-induced Fluorescence in Flame

To provide useful data and direct comparison of the single-photon and two-photon excitation schemes, the single-photon 589 nm excitation and two-photon 578 nm excitation were investigated in a sodium-doped non-premixed diffusion flame. In the gas phase environment with significant seed densities, the effects of signal trapping of 589 nm excitation are significant, and the prospect of measurements using single-photon excitation in multiphase flames is low. A direct comparison of two-photon 578 nm and 685 nm excitation is carried out on a sodium-doped flat flame burner to help determine optimal ranges of laser fluence while considering losses due to amplified spontaneous emission and ionization.

4.1.1 Single-photon Excitation

The single-photon, resonant excitation of atomic sodium at 589 nm with detection at the same wavelength is discussed first. The laser beam was focused through the sodium-doped non-premixed diffusion flame. The ICCD camera gate was 20 ns exposure and started approximately 8 ns after the laser excitation pulse. At these sodium densities, several features are notable in Figure 4.1. The time-delayed fluorescence signal shows significant attenuation along the direction of laser propagation, due to the fluorescence trapping, because the focused beam size is around 300 μ*m*.

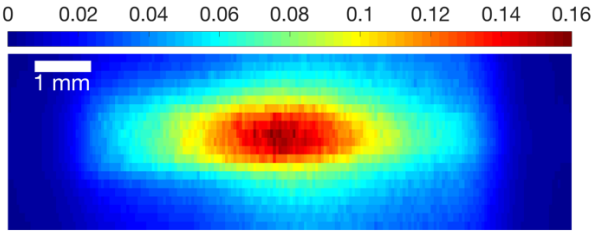

Figure 4.1 *589 nm single-photon excitation fluorescence imaging detection at the resonant wavelength, where the focused beam is 300* μm *in diameter.*

In addition, the linearity of the single photon emission at 589 nm was examined by varying the laser irradiance through the use of a waveplate and polarizer to attenuate the pump beam prior to the dye laser. The fluence dependence of the resonant emission is shown in Figure 4.2. Saturation occurs at a fluence of approximately 2×10^4 mJ/cm^2, similar to values reported by Van Calcar et al[84]. As mentioned previously, the fluorescence trapping behavior of the single-photon excitation inhibits the quantitative comparison of sodium concentration.

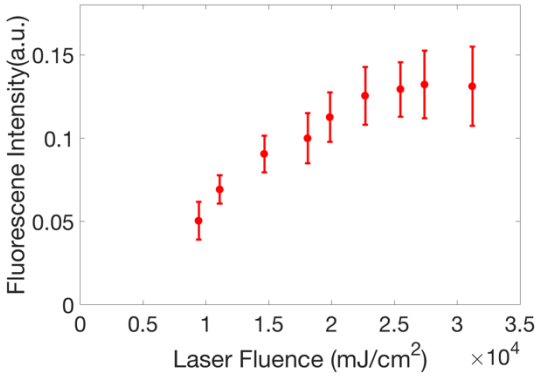

Figure 4.2 *Fluorescence intensity versus laser fluence showing fluorescence saturation at ~2×10^4 mJ/cm^2. Bars indicate one-standard deviation range.*

4.1.2 Two-photon Excitation

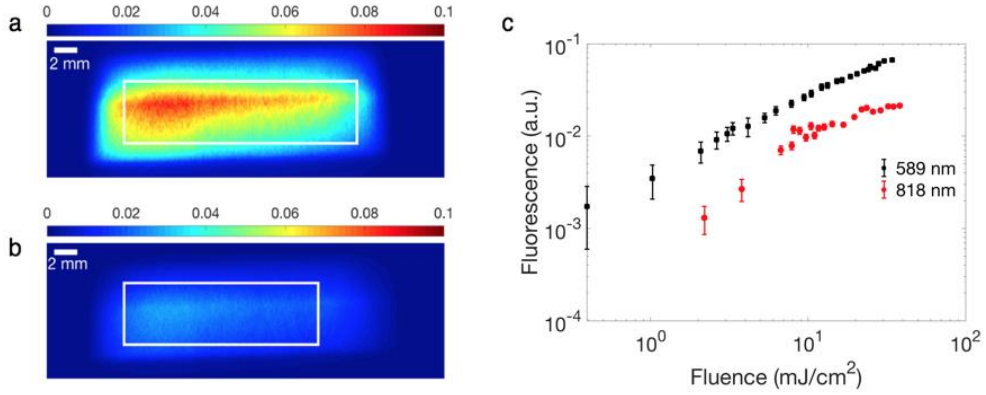

Figure 4.3 *Nanosecond two-photon 578 nm laser-induced fluorescence with detection at (a) 589 nm and (b) 818 nm with regions for signal binning indicated by the outlined areas. The fluence dependence (c) of both emission wavelengths is shown with both normalized to the peak value. Bars indicate one-standard deviation.*

Two-photon excitation of the 3s-4d transition (578 nm) was investigated as an alternative approach to minimize fluorescence trapping and evaluate the prospects for quantitative sodium concentration measurements. Due to the nonlinear process of multiphoton excitation, curves are often presented on a log-log plot, where constant slope indicates power-law behavior. For two-photon fluorescence processes, this might be expected to approach a

value of 2, with deviations explained by non-direct fluorescence emission, amplified spontaneous emission (ASE) losses, quenching processes, and ionization losses. The fluence dependence of the fluorescence, collected at a wavelength of 589 and 818 nm, is shown in Figure 4.3(c). At lower fluence, both exhibit power-law type behavior, but roll off at fluences of < 10 mJ/cm^2. The spatial distributions of both appear similar, and any non-uniformity may be accounted for by variations in the excitation laser focusing.

In order to make a direct comparison between the single- and two-photon excitation imaging in the doped sodium non-premixed diffusion flame, similar focusing was used in order to assess the role of beam attenuation and fluorescence trapping effects. Background-subtracted images for single-photon and two-photon excitation at 589 nm (3s-3p) and 578 nm (3s-4d) are shown in Figure 4.4 (a) and (b). The two laser systems used near-identical focusing and the fluorescence images are normalized to the peak signal across the shown in Figure 4.4 (c) for comparison. From this, the two-photon signal shows a much sharper gradient with fluorescence signal restricted to the excitation volume. In contrast, the single-photon excitation shows significant broadening outside of the laser focal volume which is indicative of refluorescence or signal trapping due to the resonant excitation. For comparison, the full-width half maximum (FWHM) of the fluorescence profile from single-photon excitation is 1800 μ*m* and the FWHM of the two-photon absorption laser-induced fluorescence is 400 μ*m*. The laser focusing had a beam width of ~300 μ*m* for both cases, indicating that the two-photon width is exhibiting no significant signal trapping. From this, it is clear that the two-photon excitation has greatly reduced fluorescence trapping, even for the 589 nm transition. This is interesting to note, since the ground state population is the same in both cases, and one might expect to see reabsorption effects on 589 nm emission from either process.

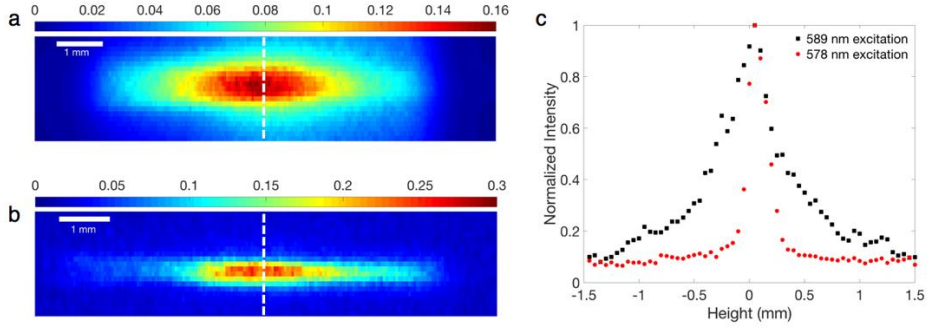

Figure 4.4 *Normalized, background subtracted images of fluorescence from the 3p-3s transition at 589nm for (a) one-photon (589 nm) excitation and (b) two-photon (578 nm) excitation with similar laser focusing. The dashed line indicates the locations for profiles across the laser focus in the fluorescence images, as shown in (c). The single photon excitation exhibits significant broadening due absorption and refluorescence, while the width of the fluorescence signal from 578 nm corresponds closely to the excitation beam width.*

Considering the level of multiphoton ionization resulting from the two-photon excitation, an ion probe was employed similar to that developed by Cool et al.[90], as shown in Chapter 3.3. The signal was acquired with a Tektronix MDO3054 oscilloscope and a 100x attenuating voltage probe (P6139B, 10MΩ). Acquisitions were typically AC coupled to minimize the contribution from the flame ionization signal, as the measure DC voltage of 1.5 V is much higher than photoionization signal of ~0.5 V. A measured voltage waveform is shown in Figure for two-photon excitation at 578 nm with a fluence of 16.7 mJ/cm^2. Wavelength scans for two different laser fluences of 1.4 mJ/cm^2 and 16.7 mJ/cm^2 are shown in Figure4.4. Both the peaks (black and red) are for 578 nm excitation (on-resonant ionization). For the low fluence case, the laser-induced ionization is absent when tuning far from the resonance, while significant REMPI signal is collected on-resonance. For the high-fluence case, the off-resonant signal is significant, made evident by the much larger spectrum width and the baseline at a signal of 5 V-μs. At the peak, the signal increases by a factor of ~4. This can be compared to the low fluence signal ratio on- and off-resonance of ~60. In both cases,

the on-resonance ionization is significant and may represent a significant loss to the fluorescence yield.

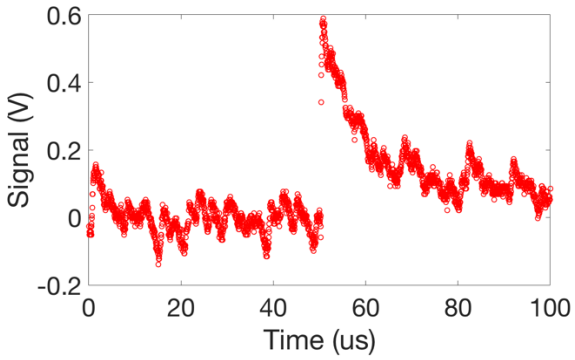

Figure 4.5 *Ionization single shot signal in premixed flat flame, 578 nm two-photon excitation, obtained with the ionization probe.*

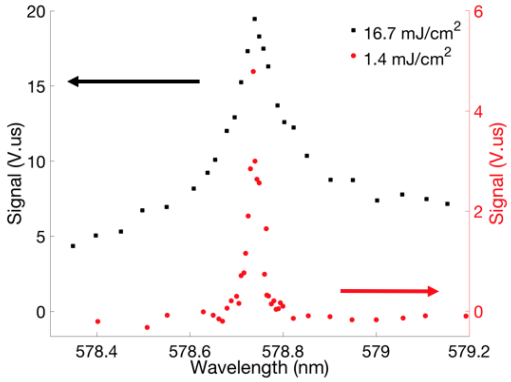

Figure 4.6 *578nm wavelength scan at two different laser fluences, 16.7 mJ/cm^2 (black) and 1.4 mJ/cm^2 (red). At low fluence, the on-resonance ionization signal is strong, while there is little laser-induced ionization off-resonance.*

Examining the 818 nm fluorescence emission of 578 nm excitation, the detected fluorescence does not originate directly from the excited 4d state. Instead, the 818 nm emission originates from the 3d state and relies on collisional transfer and non-radiative mechanisms for excitation following the two-photon pumping to the 4d state. Consideration of these processes may require a model including collisional and non-radiative transfer effects to accurately capture the dynamics and to predict yields for the 818 nm emission.

An alternative approach was identified and tested, with the same detection wavelength to test the potential for improved signal yields and more direct analysis of the involved processes. Two-photon 685 nm excitation of the 3s-3d transition leads to an excited state which is detectable by fluorescence at 818 nm. Instead of the indirect population for 578 nm excitation, for this scheme the 685 nm excitation leads to a direct emission of detectable photons. The 685 nm and 578 nm two-photon excitation schemes were tested on the premixed flat flame with $NaNO_3$/methanol seeding. Fluorescence at 818 nm was detected and is shown on a log-log scale plot in Figure 4.7, where 685 nm excitation shows significantly stronger signal levels than 578 nm, which could be caused by the direct fluorescence emission from the 3s-3p state. In addition, the noise floor for the 685 nm excitation is much higher, and exhibits less non-linearity – a potential sign of saturation of the transition at lower fluences.

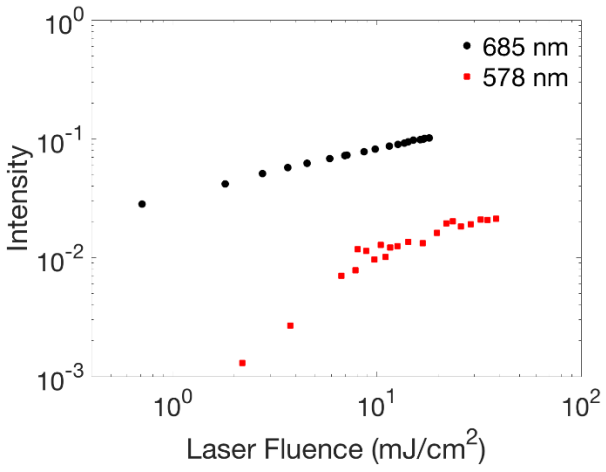

Figure 4.7 *Nanosecond two-photon 578 nm (red) and 685 nm (black) excitation with detection at 818 nm for both. The fluorescence from 685 nm excitation has stronger signal level compared with 578 nm excitation.*

For further understanding the relationship between laser energy, fluorescence, ionization and amplified spontaneous emission, 685 nm excitation was monitored in the sodium-doped flat flame burner. During these experiments, fluorescence (collected with photo-

multiplier tube), ionization level (detected by ion probe) and amplified spontaneous emission (photodiode sensors) were acquired with a boxcar integrator at 10 Hz rate. Due to the limited number of the boxcar channels, each pair of the signals were taken simultaneously while monitoring the laser energy on a shot-to-shot basis. A sample ASE signal with the boxcar integration region shown in the outlined box is shown in Figure 4.8.

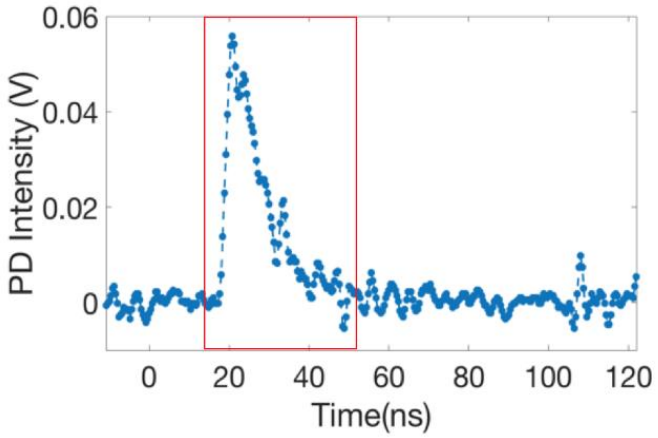

Figure 4.8 *Single shot oscilloscope trace from amplified spontaneous emission at 818 nm with two-photon excitation at 685 nm. The boxcar integrator was set to a region corresponding to the red box, with analog gain set to avoid saturation of the ASE signal on the integrator.*

Figure 4.9 indicates for 685 nm two-photon excitation, the fluence dependence of the 818 nm fluorescence, ionization level, and the amplified spontaneous emission signals. The trend for fluorescence with increasing fluence is similar to that shown before. Even at the lower range of fluences shown in this figure, the ionization level is already significant. This can be attributed to the strong cross-section for electronic excitation and the low-lying ionization state which would result in a probable 2+1 REMPI process. This designation corresponds to the 2 photons resonant with the 3s-3d transition and 1 additional photon required to reach the ionization threshold. This significant ionization behavior for sodium was noted by Weiland et al[76]. The high levels of sodium present in the seeded flames also result in significant ASE

effects, although the lowest measured range of fluence shows behavior very close to a threshold. The ASE signal variation with fluence has a general increasing trend, but there is a significant amount of scatter for every laser fluence studied. This can be attributed to the stochastic nature of the ASE wave building up, and potentially could be accounted for by a strong backward-directed ASE signal which is not monitored. One outcome of these characterization of the fluence dependence on signals is to better choose an optimal fluence for propellant experiments. The propellant flame burns last only seconds, so a thorough characterization of fluence dependence is impossible. Improved understanding of the fluorescence, ionization and ASE with laser fluence could help chose the right laser energy to maximize fluorescence yield and reduce the ionization and ASE losses. During this study, to achieve significant signal levels of fluorescence signals, ~40-50 mJ/cm^2 was chosen.

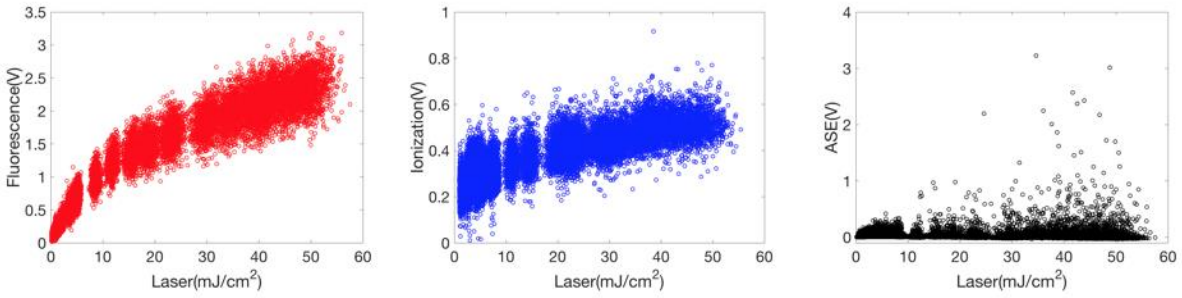

Figure 4.9 *685 nm two-photon excitation of the correlation between laser energy to fluorescence (818 nm), ionization, and amplified spontaneous emission (ASE). The $NaNO_3$ concentration was 25 g/L in the water solvent.*

4.2 LIF in Propellants Flame

To effectively image the sodium atomic concentration in the propellant flame, there are several important considerations. First, the environment is highly scattering and the high temperature particles and droplets in the flame environment can interfere with particle gray body emission. In addition, the doping levels of sodium nitrate used in these propellant

formulations are significant and may result in fluorescence trapping and beam attenuation. Single-photon and two-photon LIF were used to detect the sodium-doped propellant without microwave first. In order to examine the spatial homogeneity of ground state atomic sodium during microwave-enhanced propellant burning, two-photon excitation PLIF at 685 nm was applied.

4.2.1 Without Microwave

4.2.1.1 Single-photon Excitation

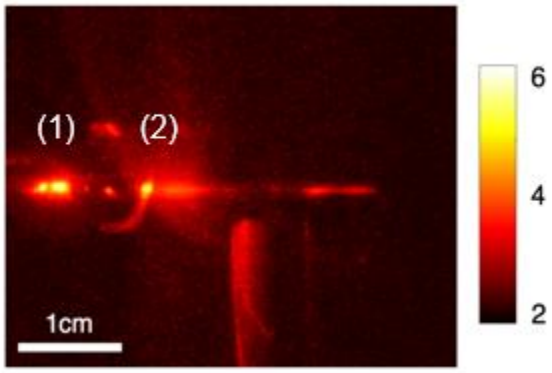

Figure 4.10 *589 nm single-photon excitation and 589 nm fluorescence of 3.5% sodium-doped aluminized propellants, normalized by the peak value and log scaling displayed on a logarithmic scale showing, strong particle scattering, attenuation, background emission and re-fluorescence.*

Sodium D1 line (589 nm) single-photon laser-induced fluorescence was investigated briefly in a sodium-doped propellant flame. A fast-gated ICCD camera with a short bandpass filter was used to capture the images, where the exposure is 20 ns duration. In these burns, there is evidence of strong particle scattering at the resonant excitation/detection wavelength, sodium background emission, and fluorescence trapping as demonstrated in Figure 4.10. The laser tuned to 589 nm was focused to a line width 300 μ*m* through the 3.5% $NaNO_3$ doped, aluminized propellant flame from left to right, and the fluorescence was detected at the resonant wavelength of 589 nm. Strong particle scattering is evident in Figure 4.10 at location

(1) from aluminum particles or agglomerate, and the laser line fluorescence trapping could be noticed clearly in the region (2). In this case, the scattering is so strong that it shows up clearly throughout the images as scattering takes off additional surfaces. Because of these complications, single-photon resonant laser-induced fluorescence is ill-suited for measurements in the multiphase propellant combustion environment.

4.2.1.2 Comparison of One-photon and Two-photon LIF in Propellant Flames

To avoid particle scattering interference and signal trapping effects, two-photon excitation has already shown advantages in the sodium-doped flame conditions. Investigation of 578 nm and 685 nm excitation in propellant flames are presented in this section. Based on the results from the gas phase sodium-seeded flame, a fluence for the operation was chosen based on the data amplified spontaneous emission, ionization, and fluorescence in section 4.1.2.

The excitation at 578 nm showed promising results in gas phase flame testing, so initial experiments examined burning in sodium-doped propellant flames. A summary result from a 3.5% $NaNO_3$, aluminized strand burn is shown in Figure 4.11(a). The image is shown on a logarithmic scale to highlight the total dynamic range in the image. The image quality is far better than the case of the single-photon resonant excitation, but there are strong interferences from particles in multiple locations which are comparable to the background sodium fluorescence level. A profile along the white line shows a slice through a region with few particle interferences. The signal-to-noise ratio (SNR), defined as the mean signal level in the highlighted box divided by the standard deviation of the signal over the same area in the image ($SNR = \mu/\sigma$) was approximately 10 for the case shown in Figure 4.11(a).

The second two-photon excitation scheme considered was excitation at 685 nm for the 3s-3d transition. Unlike the 3s-4d excitation, the 3d state has a detectable, directly-emitted

photon at 818 nm. Due to this direct access to the excited state of the detectable photon, signal levels were anticipated to be significantly higher than the two-photon 578 nm excitation. The fluorescence imaging result in a similar propellant burn and fluence level of 55 mJ/cm^2 is shown in Figure 4.11 (b). The image quality is superior, with an SNR of 112 over the highlighted box. Again, the signal quality is shown by plotting the signal on a log-scale along a vertical line in the image, shown in the right panel. The small jump in signal in the line plot is due to a particle interference. In addition, the signal quality and rejection of background particle level were superior. This scheme (3s-3d excitation at 685 nm; detection of 3d-3p at 818 nm) offers the possibility of sodium atom mapping in high Na density, highly scattering environments such as aluminized composite-propellant flames.

An additional consideration is the loss due to ASE on the 818 nm fluorescent emission. A photodiode was placed after the laser sheet passed through the test section and a dichroic beamsplitter and bandpass filter were used to ensure only 818nm light was collected. Particularly at high dopant levels, ASE was observed even at fluences which did not exhibit any detectable gas phase flame ASE. The presence of ASE on such strong oscillator strength transitions (alkali atoms) is likely unavoidable at these very high atomic concentrations. No signal depletion in the fluorescence images was evident in the test burner (at a lower concentration), but these effects have not been quantified. Although particle interference is present, the scheme offers the potential for qualitative mapping of the atomic sodium concentration. To reduce the blackbody emission, an ultra-narrow (FWHM 2nm) bandpass filter was applied to detect 818 nm fluorescence excited by 685 nm within microwave condition. Burns with aluminum content but no sodium dopant exhibit signal levels which are on the order of ~200 to 300 counts – well below the observed signal levels from TALIF

excitation at 685 nm. As a result, any strong signal observed in the fluorescence images is attributed to the presence of sodium.

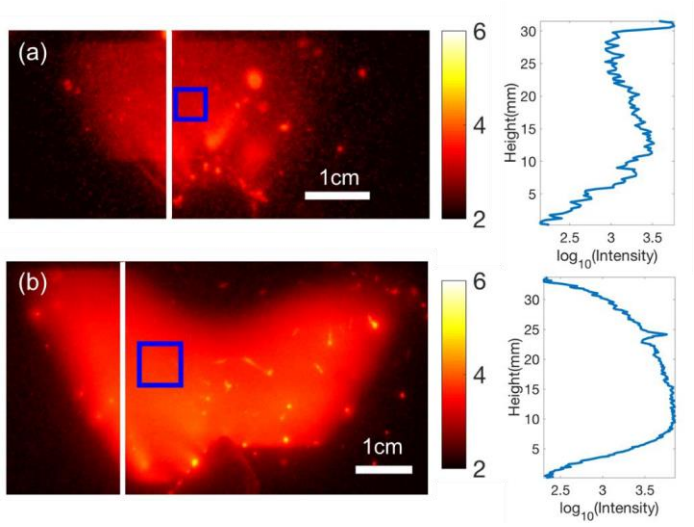

Figure 4.11 *Comparison of 578 nm (3s-4d) and 685 nm (3s-3d) two-photon ground state sodium fluorescence of 3.5% $NaNO_3$, aluminized composite propellant burning. Both are in natural log scaling. (a) 578 nm excitation at a fluence of 52 mJ/ cm^2; (b) 685 nm excitation at fluence of 55 mJ/ cm^2.*

As discussed in Chapter 2, information about the propellant flame structure is important to understand the various mechanisms of propellant combustion. Based on the advantages of 685 nm two-photon laser-induced fluorescence discussed above, this excitation scheme was used for fluorescent imaging of the sodium distribution in a number of propellant flame formulations and burns. Figure 4.12, shows sodium-doped propellant flame structure of 818 nm fluorescence emission for a 1% and 3.5% $NaNO_3$ dopant in the aluminized composite propellant flame. The sodium distributions appear to be quite diffuse, with no significant changes between the two formulations. Based on these images, it appears that the $NaNO_3$ has undergone decomposition rapidly at the burning surface. Looking at the fluorescent images in Figure 4.12, there is some evidence of non-uniform distributions of sodium near the burning

surface. Another higher magnification sequence of images of a 3.5% $NaNO_3$ aluminized propellant strand burning is shown in Figure 4.13. Near the burning surface, there are localized high concentration regions of sodium. These are likely originating from $NaNO_3$ crystals decomposing at the burning surface. The $NaNO_3$ crystal size after milling to formulate the composite propellant is unknown, but could be further examined with sectioning and microimaging. In these images, to approve the sodium distribution at the burning surface. The images intensities are lower due to the high magnification collection angle, but sufficient signal is shown to identify sodium near-surface distributions.

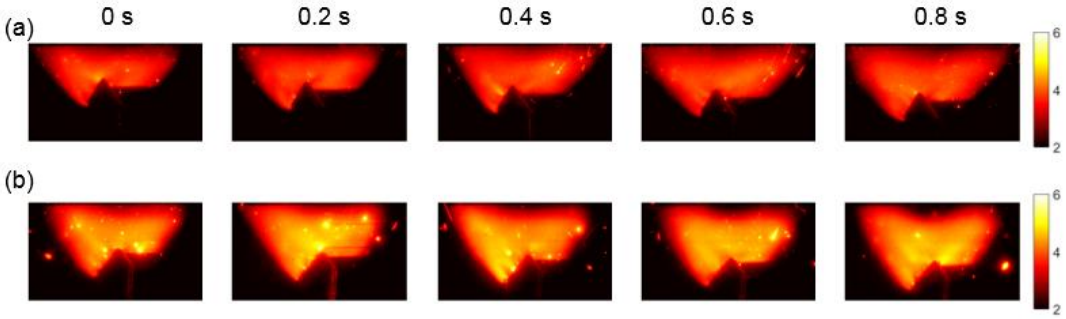

Figure 4.12 *685 nm two-photon excitation in different sodium-doped propellant flame and 818 nm emission images in natural log of normalized intensity. (a) 1% $NaNO_3$ doped propellant flame structure in sequence; (b) 3.5% $NaNO_3$ doped propellant flame structure in sequence.*

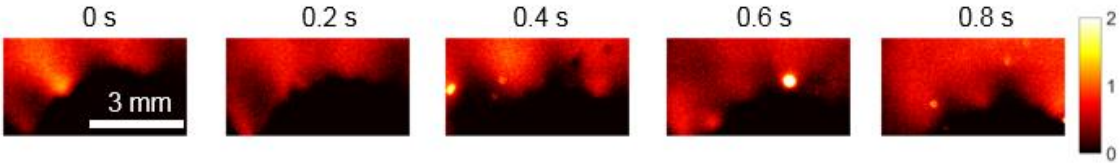

Figure 4.13 *685 nm two-photon excitation in 3.5% sodium-doped propellant flame and 818 nm emission images at higher magnification in natural log of normalized intensity, where indicated more clear of the sodium distribution at the burning surface.*

Strong 589 nm emission has been observed from the sodium doped propellant flame before through imaging and emission spectroscopy. However, compared with directly measure

589/818 nm emission imaging, two-photon LIF also has the advantage of measuring ground-state atomic sodium, which could help inform the microwave effects on increasing ground-state sodium concentration in propellant flame. The differences between the two flame structures are shown in Figure 4.13, due to the fluorescence was showing ground state atomic sodium distribution and 589 nm emission shows the 3p state atomic sodium. From this example image comparison, it appears that there is a region of significant sodium concentration (Figure 4.14) which does not appear in the filtered emission imaging. Since these structures are diffuse, we might infer that there is significant sodium population in lower temperature regions of the propellant flame which are not appearing in the synchronized emission at 589 nm.

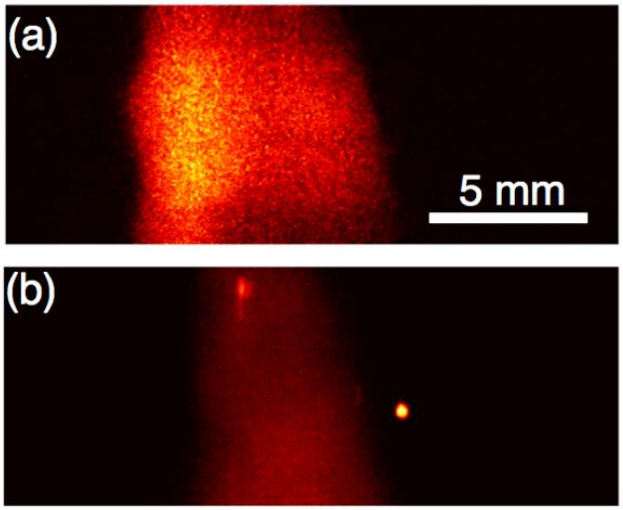

Figure 4.14 *Synchronized 685 nm TALIF 818 nm emission and 589 nm emission images to show the particle emission could be reduced by using ultra-narrow bandpass filter. (a) TALIF imaging, (b) 589 nm emission imaging.*

4.2.2 With Microwave

4.2.2.1 Burning Rate Enhancement

Backlit images were used to infer the propellant burning rate for four different propellant formulations as previously described in Chapter 3. Three strands of each formulation were burned without the microwave field and with the microwave field at a duty

cycle of 100%, 50%, and 30%. The burning rate enhancement, as reported in Table 4-1, is defined based on normalized burning rate (enhancement = $(R_{MW} - R_0)/R_0$). R_{MW} is the measured burning rate with different duty cycle microwave condition and R_0 is the burning rate without field applied. The results show a significant burning rate enhancement (>40%) with high sodium dopant levels at 100% microwave duty cycle. As previously shown, the addition of aluminum also leads to an enhancement of burning rate with microwave field. The average burning rates for the 30% and 50% duty cycle case are consistent with these trends.

Table 4.1 *Propellant burning rate enhancement with microwave field application.*

Formulation Name	**Microwave duty cycle**		
	100%	**30%**	**50%**
Al-AP-$NaNO_3$ 3.5%	**47%**	**15%**	**20%**
Al-AP-$NaNO_3$ 1.0%	**20%**	**9%**	**10%**
AP-$NaNO_3$ 3.5%	**44%**	**10%**	**17%**
AP-$NaNO_3$ 1.0%	**6.5%**	**3.1%**	**N/A**

To monitor the degree of coupling to the propellant flame during strand burning, forward and reflected microwave power measurements were taken. Figure 4.15 (a) shows the forward and reflected power during a single strand burning of 3.5% $NaNO_3$ doped aluminized propellant 100% duty cycle. Time zero in this figure 4.15(a) indicates the start time of the microwave, not the beginning of the burn (it is ignited 1 s prior to the start time). At this point, the propellant burn should be nearly steady state. For the first 15 seconds, while the burn is in progress, the reflected power is near zero. This indicates strong absorption to the propellant strand and propellant flame. Coupling during this phase may take place as proposed in Chapter 2 and detailed by Barkley et al.[9] Energy deposits in the condensed phase strand, the high temperature condensed-phase products through absorption to aluminum-oxide, or with the gas-

phase flame through free electrons impact with neutrals which are likely liberated from the sodium vapor. The second panel, Figure 4.15 (b), shows the normalized absorption (A) based on forward and reflected power. This is defined as $A = (P_f - P_r)/P_f$, where P_f is the forward power and P_r is the reflected power. The majority of the imaging data considered is only during a few-second time interval from approximately ~5-7 s where the propellant has reached steady state burning. Another forward and reflected energy measurement from the diodes for 30% duty cycle of microwave and 1 Hz repetition, is shown in Figure 4.16.

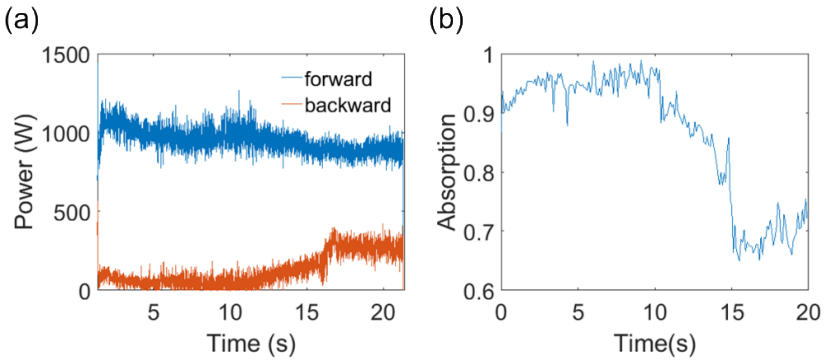

Figure 4.15 *(a) Microwave forward and reflected power monitored with Schottky diodes with a directional coupler. (b) Normalized absorption for the duration of the propellant burning.*

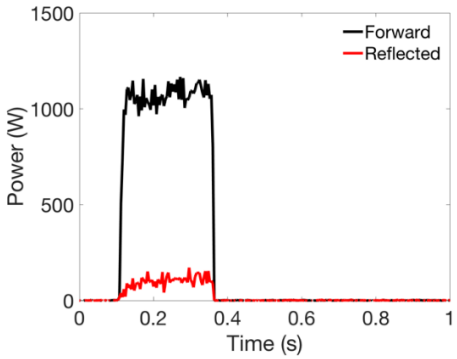

Figure 4.16 *Calibrated Schottky diode trace to measure forward and backward power at 30% duty cycle for burning of a 3.5% $NaNO_3$ doped aluminized propellant strand.*

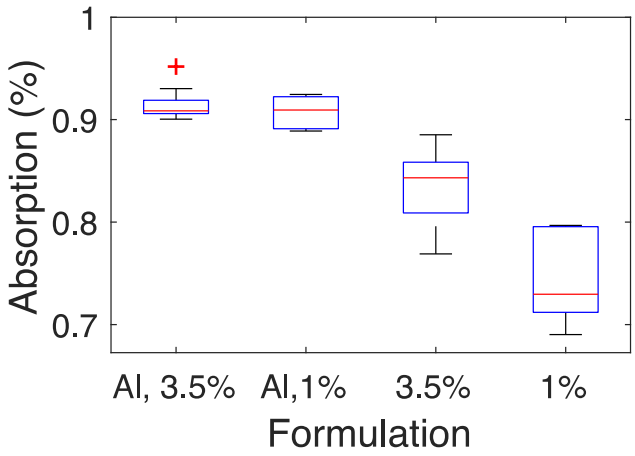

Figure 4.17 Microwave power absorption of *different propellant formulation during 30% duty at 1 Hz. For each box, the median is indicated by a red line, the box indicates the 25-75% range of data, the whiskers indicate the full range of values, and outliers beyond ±2.7σ are indicated by the symbol '+'. (need another 50% duty cycle here).*

The comparison of absorbed microwave energy for the various formulations is presented in Figure 4.17. For each case, the data shown is for a 30% duty cycle microwave. First, comparing the case of 3.5% sodium doping with and without aluminum, we see stronger absorption for the aluminized case. Second, the content of sodium varying from 1% to 3.5% seems to be relatively negligible in contributing to additional microwave energy absorption. Third, the addition of sodium from 1% to 3.5% without the presence of aluminum promotes a significant increase in microwave energy absorption. Finally, with these changes in absorption, we should also consider the relative increase of the burning rate with microwave application. Although the absorption is approximately the same for the aluminized 1% and 3.5% dopant cases, the burning rate increase is 15% versus 9%, respectively. Comparing the cases of 3.5% dopant with and without aluminum, we again see a 15% increase in burning rate versus a 10% increase in burning rate. To summarize, both the aluminum content and sodium dopant level are contributing to increased microwave absorption, but the addition of both is promoting additional increases in flame speed without altering the amount of absorbed microwave energy.

This suggests that the mechanisms for absorption detailed in Figure 4.17 are important, but may have significantly different effects on the magnitude of the burning rate modification.

4.2.2.2 Image Registration

To examine differences in the ground-state versus excited-state sodium distribution during the microwave-enhanced propellant burning rate, an emission image and two-photon 685 nm excitation PLIF were taken simultaneously. To directly compare the two images, a registration procedure was used so that particle interferences could be inferred in both images. A registration test chart taken by two cameras was used for image registration by using Scale-Invariant Feature Transform (SIFT) algorithms built in MATLAB code (see appendix). SIFT is an algorithm in computer vision to detect and describe local features in images, was described by Lowe et al[85]. Due to variation in intensity across each image, the first step was to normalize the initial images as shown in Fig 4.18 (a) for the PI ICCD camera and (b) for the Photron high-speed CMOS camera. The SIFT method is applied to register images and the overlapped image is shown in Fig (c). The matrix is saved to further apply to the PLIF and emission imaging as shown in Figure 4.18.

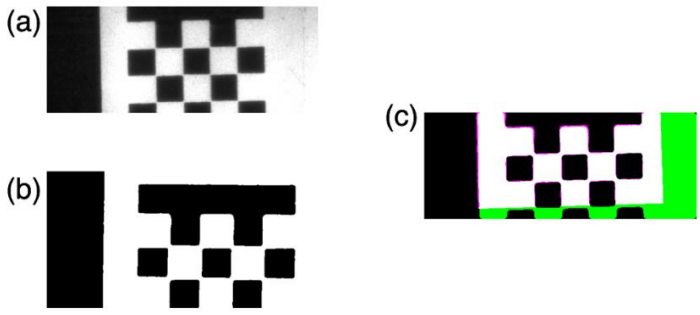

Figure 4.18 *SIFT methods of registration of two different intensities images. (a) PI-ICCD image; (b) Photron high-speed image; (c) registered overlapped image (red for (a) and green for (b), black for registered area.*

To make a direct comparison between the TALIF image and backlit image or the TALIF and emission images, cameras were synchronized as previously described and the trigger data was recorded on the oscilloscope to confirm frame synchronization. An example of the result of applying the transformation matrix to the PLIF and emission images is shown in Figure 4.18. Panel (a) and (b) show the TALIF and emission images, respectively. Panel (c) shows both images overlaid, where the white region indicates the same region seen in both images. A good correspondence is seen for the global structure, although differences are apparent and can be attributed to the planar slice of the three-dimensional flame structure as well as variations in emission which may be temperature-dependent. The next section will compare the observed differences of the fluorescence and emission flame structures.

4.2.2.3 Two-photon PLIF at Different Duty Cycles

In the results presented here, the microwave is modulated at 0%, 30%, 50%, and 100% while varying the aluminum content of solid propellant as well as the level of $NaNO_3$.

(a) TALIF with backlit images to track the flame surface

Backlit images and fluorescence images were synchronized and registered under 30% microwave duty cycle experiments. The backlit images shown here are normalized by the background light and binarized by thresholding to visualize particulate matter above the burning surface and allow measurement of burning surface location. In addition, by directly comparing the backlit images to the sodium fluorescence maps, there are regions of increased signal which correspond to particulates. The first series presented in Figure 4.19 shows a comparison of the sodium TALIF with and without microwave field for two separate propellant burning events. Examining these images, the signal level is significantly higher with the applied microwave field (bottom series). ‘Blooming’ events appear diffuse in the fluorescence images and result in a signal increases of 10-20 times in

the microwave illuminated cases. Although some signal levels seem to correspond with the presence of condensed phase particles (aluminum droplets), the strongest fluorescence features in the flames corresponding to 0.2 and 0.6 s are not correlated with any large condensed phase particulate. This is consistent with the observation from the fluorescence signals that these features are diffuse. These initial studies show a series of interesting phenomena including local variation in the sodium density, but the limited magnification and low acquisition speed complicate interpretation of the effect of microwave application on the sodium distribution.

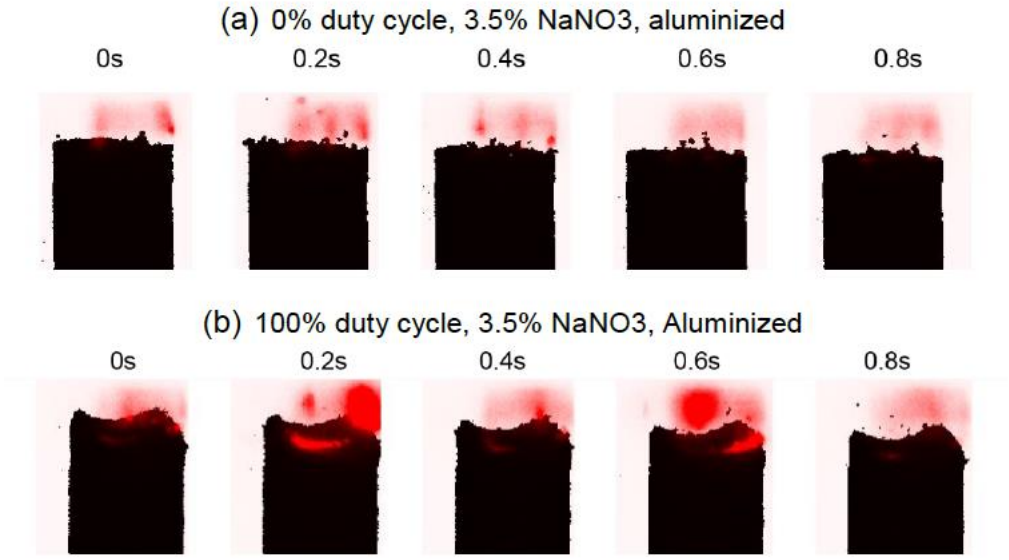

Figure 4.19 *Comparison of sodium laser-induced fluorescence levels during propellant burning with no applied microwave field and with 100% duty cycle applied field.*

Based on the qualitative increase in the fluorescence signal intensity during microwave coupling, we wanted to determine if the level of sodium was increasing. By directly interrogating the ground state with the two-photon LIF technique and observing at 818 nm, a qualitative observation of the ground state Na population was made with and without microwave application. To quantify the Na fluorescence intensity changes during 30% duty

cycle modulation, the fluorescence signal was integrated over each frame with background subtraction, keeping track of the sequence of microwave application. Although the process is stochastic, this was averaged over 17 microwave cycles and 3 propellant burns. The range of the signals in these frames is shown in Figure 4.20, where red lines indicate the median, the boxes indicate the middle 50% of observations, with the extremes shown by the whiskers. The microwave field is only applied for the frames at 0.2s and the average signal levels are shown for no microwave application and 100% and 0% duty cycle application for comparison. There is a clear increase in fluorescence signal which can be attributed to an increase of the local concentration of ground state atomic sodium. This increase may be promoted by an increased flux (increasing burning rate) or some local enhancement due to the modulated field.

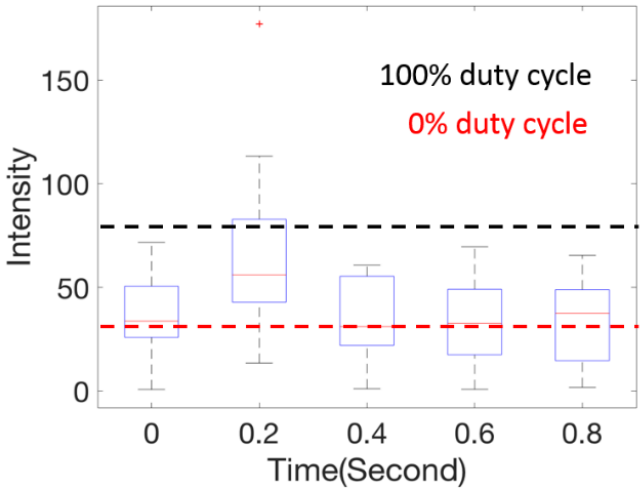

Figure 4.20 *Na fluorescence intensity for low duty cycle microwave application. Black and red lines show the 100% and 0% duty cycle average fluorescence intensity. For each box, the median is indicated by a red line, the box indicates the 25-75% range of data, the whiskers indicate the full range of values, and outliers beyond ±2.7σ are indicated by the symbol '+'.*

Similar phenomena are observed in the case of non-aluminized propellant burning in the microwave field. Quantitative comparison of the propellant PLIF average intensity during the burning is shown in Figure 4.20 for the four formulations previously discussed.

Background emission shows the microwave run at 100% duty cycle without laser excitation taken by the same conditions as the ICCD camera to show the magnitude of 818 nm emission that may interfere with the collected PLIF signal. The general trends can be summarized for all cases as an increase in the ground state sodium concentration with microwave application. Comparing the same level of dopants with and without aluminum, the approximate increase in sodium fluorescence is comparable. Overall, the higher dopant concentration and higher level of aluminum lead to the promotion of the sodium fluorescence signal. This may be an indication of a feedback mechanism as the presence of increased sodium in the un-enhanced flame leads to higher background levels of free electrons. These more readily lead to additional energy absorption, which then leads to increase heating and additional ionization.

To summarize these observations with two-photon sodium PLIF in propellant flames: (1) the microwave application increases the ground state sodium distribution in the flame. (2) Aluminized and varying dopant levels in the propellant flames are also tied to shifts in the average increase of the sodium fluorescence signals. (3) At similar levels of sodium doping, the presence of aluminum also leads to relative increases in the amount of ground state sodium. Taken together, the increase in sodium seems to be driven by an interplay between sodium-dopant and aluminum content. This complementary picture is consistent with the burning rate observations presented by Barkley et al.[9] and in the early discussion in this dissertation.

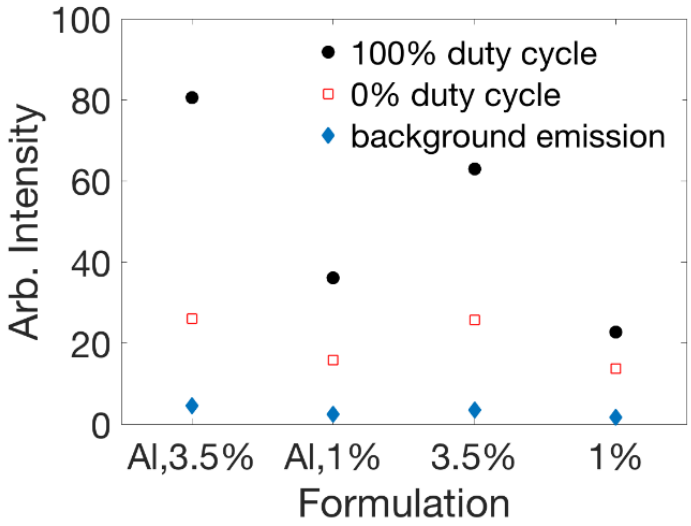

Figure 4.21 *Comparison of two-photon PLIF fluorescence intensity for different propellant formulations with and without microwave application.*

(b) TALIF with Na Emission

Based on the 30% duty cycle, 3.5% sodium doped propellant results shown in Figure 4.19, the phase-averaged increase in the sodium fluorescence signal was evident. For a series of burns, strong Na fluorescence signal was observed with some degree of repeatability, but the low-sampling rate and small number of laser shots acquired during a single burn complicate the analysis of the "blooming" events that are observed. This section focuses on the use of a high-repetition-rate sodium emission imaging in combination with 10 Hz TALIF images at increased magnification to inform the origin of the local increases in sodium concentration that are tied to the microwave field application.

'Blooming' events were shown in the previous section, but due to the lower magnification of the fluorescence images, little detailed structure is evident. The 685 nm two-photon excitation scheme was used with at a magnification 3X higher than the previous results shown. Simultaneous high-speed (1 kHz) 589 nm emission images were taken for each burn. Synchronized frames from the magnified fluorescence images and 589 nm emission images

are shown in Figure 4.22 and Figure 4.23 during the same burning of 3.5% $NaNO_3$ doped aluminized propellant, at 100% microwave duty cycle.

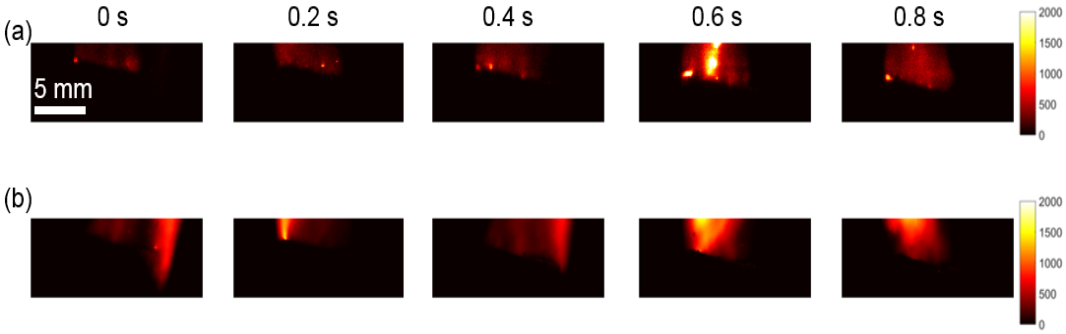

Figure 4.22 *Synchronized images of 3.5% $NaNO_3$ doped aluminized propellant flame, 100% microwave duty cycle, at the burning surface. (a) 685 nm two-photon excitation and 818 nm fluorescence detection; (b) 589 nm emission images.*

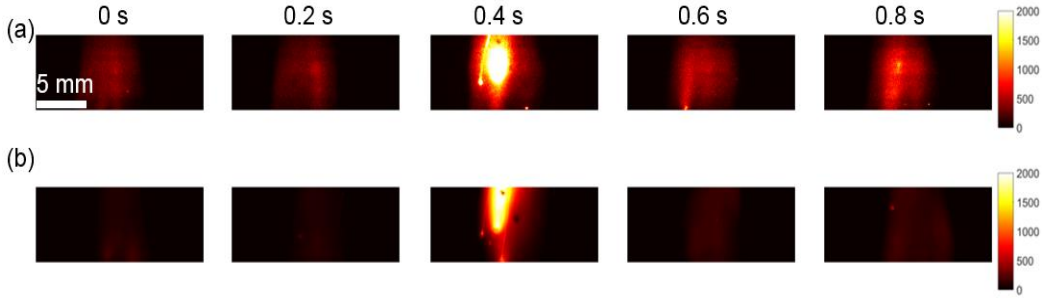

Figure 4.23 *Synchronized images of 3.5% $NaNO_3$ doped aluminized propellant flame, 100% microwave duty cycle, same burn as Figure 4.22. (a) 685 nm two-photon excitation and 818 nm detection; (b) 589 nm emission images.*

By rescaling the 'blooming' events in Figure 4.24, it appears the strongest signal region in the PLIF image corresponds closely to a region where agglomerates are occupying (indicated by a shadow in the 589 nm emission image). From these images, there is a good correspondence between particles in both images, although fewer particles are evident in the fluorescence image. This is attributed to the narrow laser sheet used in these studies. As compared to cases with no sodium addition in aluminized propellants with laser illumination, these signal levels are much higher than can be attributed to particle scattering interference

through the filter. As a result, the strong signals originating from these particulates are likely agglomerates of $NaNO_3$ which have been ejected from the propellant burning surface. The mechanisms for this are still unclear, but this has been observed only for cases with microwave illumination. Synchronized fluorescence and high-speed emission images at 1 kHz indicate the plasma kernel formation, as shown in Figure 4.25.

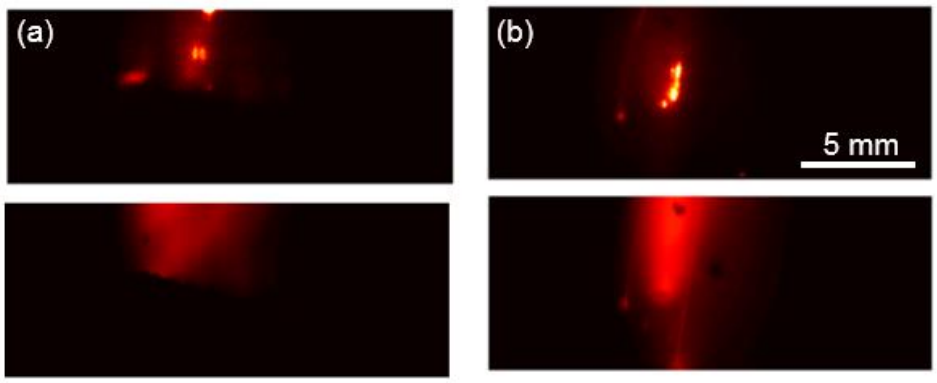

Figure 4.24 *Rescaling of Figure 4.22 and Figure 4.23 'Blooming' events. (a) Figure 4.22 at 0.6 s; (b) Figure 4.23 at 0.4 s. Images in the top row show fluorescence and the bottom row show path-integrated emission.*

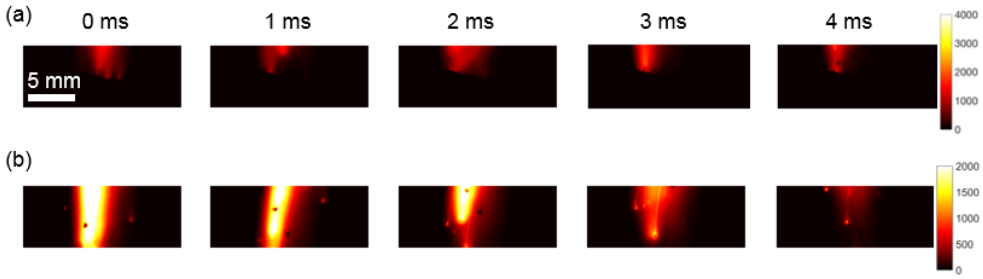

Figure 4.25 *1 kHz high-speed videos of path-integrated emission in sequence. (a) It shows the same events at 2 ms as Figure 4.24 (a); (b) It shows the same events at 2 ms as Figure 4.24 (b).*

4.3 Discussion

Characterization of sodium atomic distribution in alkali-doped propellant flames has been made through single-photon and two-photon laser-induced fluorescence schemes. The

two-photon (3s-3d, 685 nm), direct fluorescence emission from 3s-3p (818 nm), resulted in excellent signal-to-noise ratios of >100 with limited interference from particle emission and scattering. This scheme should allow qualitative maps of ground-state atomic sodium distribution in high optical density and high particle scattering environments.

From the observation of increased atomic sodium concentration during the microwave applications, it is apparent that there may be opportunities for improving performance in the microwave absorption process by changing propellant formulation. Higher magnification TALIF imaging help characterize the ‘blooming’ events with the registered imaging of 589 nm emission imaging. It is of great interest to examine these effects in a more repeatable solid propellant flame configuration (either local diffusion or monopropellant flames) by modifying the propellant surface geometry to better capture effects with the laser-based fluorescent imaging. The addition of high-speed emission imaging and high-speed backlit imaging in combination with low-speed fluorescence imaging provides detailed information on the evolution and origin of regions high local sodium concentration.

CHAPTER 5. CONCLUSIONS

This dissertation presented experimental data showing the potential for a new two-photon excitation scheme for fluorescence mapping of atomic sodium in environments that exhibit high levels of scattering and are at significant sodium concentrations. These environments exhibit particular challenges for measurement including the high level of scattering due to the multiphase combustion phenomena, the transient variation in flame structures, the requirement for single-shot imaging capability, and the high levels of sodium concentration. A series of studies in gas-phase flames were used to characterize the excitation schemes, and promising strategies were investigated in multiphase composite solid propellant combustion.

Comparisons were made with single-photon and a two-photon excitation scheme in gas phase flames to examine the role of potential losses due to ASE, ionization, and quenching. A stable flame, generated by a premixed flat flame burner with a nebulizer, allows for the investigation of nanosecond single-photon and two-photon laser-induced fluorescence signals with the goal of quantitative measurements at high sodium doping levels. Two-photon LIF excitation (at 578 nm and 685 nm) has the advantage of avoiding fluorescence trapping or re-emission as compared with single-photon excitation. In addition, both of the two-photon LIF detection schemes investigated thus far show promise of reducing interferences from laser scattering due to the non-resonant excitation and detection wavelengths. Ionization and ASE were characterized as a function of fluence for both excitation schemes and offer a series of datasets that will allow the application of a rate-equation model to the system in order to assess the level of saturation and signal losses due to ASE, ionization, and quenching. Significant on-resonance ionization signals were detected with an ion probe and it was shown that off-

resonance ionization was below the detection limit at low fluences. In particular, the non-direct excitation of the original states of the observed 589 nm and 818 nm emission complicate the analysis of fluence dependence data without additional kinetic rate modeling. Two-photon excitation from 3s-4s (685 nm) has better fluorescence signal to noise compared the excitation of 3s-5s (578 nm) due to the collection of direct fluorescence emission from 3d-3p states (818 nm).

Progress towards characterization of the sodium atomic distribution in alkali-doped propellant flames has been made through the introduction of a two-photon laser-induced fluorescence excitation scheme. This scheme resulted in excellent signal-to-noise ratios of >100 with limited interference from particle emission and scattering. This scheme should allow qualitative maps of sodium atom distributions in high optical density (high atomic density) environments. The two-photon excitation and one-photon emission limits signal-trapping effects and yields high signal levels with good discrimination from the background.

The prospects for qualitative imaging of the atomic sodium distribution in plasma-enhanced, sodium-doped propellant flames are high, and initial studies showed increases in the sodium level during the presence of the microwave field. From the observation of increased atomic sodium concentration during the microwave field application, it is apparent that there may be opportunities for improved performance in the microwave absorption process in propellant formulation. It is of great interest to study the time-decay of the atomic sodium levels in these propellant flames following the turn-off of the applied microwave field. By determining the time to return to the steady-state non-microwave burning case, strategies for improved interactions utilizing less applied power may be realized.

Additionally, investigation of the distribution of atomic sodium relative to the propellant flame structure (both diffusion and premixed flame structures) will be necessary to account for the magnitude of the energy-coupling processes in microwave-enhanced composite propellant burning. In combination with sodium planar imaging, fluorescence imaging of OH and CN in the propellant flame environment may help elucidate the spatial location of microwave plasma initiation and lead to improved understanding of the plasma-enhanced propellant burning process.

REFERENCES

1. Dayton, D. C., French, R. J. & Milne, T. A. Direct Observation of Alkali Vapor Release during Biomass Combustion and Gasification. 1. Application of Molecular Beam/Mass Spectrometry to Switchgrass Combustion. *Energy & Fuels* **9,** 855–865 (1995).
2. *Assessment of coal gasification/hot gas cleanup based advanced gas turbine systems: Greenfield assessment. Final report*. (1991). doi:10.2172/10132284
3. Vick, R. L., Hazlewood, C. F. & Nichols, B. L. Distribution of potassium, sodium, and chloride in canine Purkinje and ventricular tissues. Relation to cellular potential. *Circ. Res.* **27,** 159–69 (1970).
4. Browner, R. F. & Winefordner, J. D. Measurement of flame temperatures by a two-line atomic absorption method. *Anal. Chem.* **44,** 247–252 (1972).
5. Miles, R. B., Udd, E. & Zimmermann, M. Quantitative flow visualization in sodium vapor seeded hypersonic helium. *Appl. Phys. Lett.* **32,** 317–319 (1978).
6. Daily, J. W. & Chan, C. Laser-induced fluorescence measurement of sodium in flames. *Combust. Flame* **33,** 47–53 (1978).
7. Sutton, G. P. (George P. & Biblarz, O. *Rocket propulsion elements*.
8. Fabignon, Y. *et al.* Instabilities and pressure oscillations in solid rocket motors. *Aerosp. Sci. Technol.* **7,** 191–200 (2003).
9. Barkley, S. J. *et al.* Microwave-Supported Plasma Combustion Enhancement of Composite Solid Propellants Using Alkali Metal Dopants. doi:10.2514/6.2016-0685
10. Barkley, S. J., Zhu, K., Michael, J. B. & Sippel, T. R. Pulsed Microwave Enhancement of Doped Composite Solid Propellants. doi:10.2514/6.2017-0832
11. Edwards, T., Weaver, D. P. & Campbell, D. H. Laser-induced fluorescence in high pressure solid propellant flames. *Appl. Opt.* **26,** 3496 (1987).
12. Parr, T. & Hanson-Parr, D. RDX/GAP/BTTN propellant flame studies. *Combust. Flame* **127,** 1895–1905 (2001).
13. Beckstead, M. W., Puduppakkam, K., Thakre, P. & Yang, V. Modeling of combustion and ignition of solid-propellant ingredients. *Prog. Energy Combust. Sci.* **33,** 497–551 (2007).
14. Hanson, R. K. Combustion diagnostics: Planar imaging techniques. *Symp. Combust.* **21,** 1677–1691 (1988).
15. Peuker, J. M., Lynch, P., Krier, H. & Glumac, N. On AlO Emission Spectroscopy as a Diagnostic in Energetic Materials Testing. *Propellants, Explos. Pyrotech.* **38,** 577–585 (2013).
16. Yang, R. *et al.* Diagnostics of flame temperature distribution of solid propellants by spectrographic analysis. *Combust. Flame* **145,** 836–844 (2006).
17. McNesby, K. L., Wolfe, J. E., Morris, J. B. & Pesce-Rodriguez, R. A. Fourier transform Raman spectroscopy of some energetic materials and propellant formulations. *J. Raman Spectrosc.* **25,** 75–87 (1994).
18. Stufflebeam, J. H. & Eckbreth, A. C. CARS Diagnostics of Solid Propellant Combustion at Elevated Pressure. *Combust. Sci. Technol.* **66,** 163–179 (1989).
19. Eckbreth, A. *Laser diagnostics for combustion temperature and species*. (1996).

20. Hedman, T. D., Groven, L. J., Cho, K. Y., Lucht, R. P. & Son, S. F. The diffusion flame structure of an ammonium perchlorate based composite propellant at elevated pressures. *Proc. Combust. Inst.* **34,** 649–656 (2013).
21. van Eyk, P. J., Ashman, P. J., Alwahabi, Z. T. & Nathan, G. J. Quantitative measurement of atomic sodium in the plume of a single burning coal particle. *Combust. Flame* **155,** 529–537 (2008).
22. Goldsmith, J. E. M. Two-photon-excited stimulated emission from atomic hydrogen in flames. *J. Opt. Soc. Am. B* **6,** 1979 (1989).
23. Aldén, M., Goldsmith, J. E. M. & Westblom, U. Two-photon-excited stimulated emission from atomic oxygen in flames and cold gases. *Opt. Lett.* **14,** 305 (1989).
24. Haumann, J., Seitzman, J. M. & Hanson, R. K. Two-photon digital imaging of CO in combustion flows using planar laser-induced fluorescence. *Opt. Lett.* **11,** 776 (1986).
25. Kohse-Höinghaus, K., Barlow, R. S., Aldén, M. & Wolfrum, J. Combustion at the focus: Laser diagnostics and control. *Proc. Combust. Inst.* **30 I,** 89–123 (2005).
26. Hancock, R. D., Bertagnolli, K. E. & Lucht, R. P. Nitrogen and hydrogen CARS temperature measurements in a hydrogen/air flame using a near-adiabatic flat-flame burner. *Combust. Flame* **109,** 323–331 (1997).
27. Allen, M. G. Diode laser absorption sensors for gas-dynamic and combustion flows. *Meas. Sci. Technol.* **9,** 545–562 (1998).
28. Bachalo, W. D. Experimental methods in multiphase flows. *Int. J. Multiph. Flow* **20,** 261–295 (1994).
29. Beckstead, M. W., Derr^, R. L. & Price, C. F. A Model of Composite Solid-Propellant Combustion Based on Multiple Flames. *AIAA J.* **8,**
30. Hedman, T. D. *et al.* Experimental observation of the flame structure of a bimodal ammonium perchlorate composite propellant using 5 kHz PLIF. *Combust. Flame* **159,** 427–437 (2012).
31. NIST Chemistry WebBook. Available at: https://webbook.nist.gov/chemistry/. (Accessed: 26th March 2018)
32. Vanderhoff, J. A. Species profiles in solid propellant flames using absorption and emission spectroscopy. *Combust. Flame* **84,** 73–92 (1991).
33. Parigger, C. G., Woods, A. C., Surmick, D. M., Donaldson, A. B. & Height, J. L. Aluminum Flame Temperature Measurements in Solid Propellant Combustion. *Appl. Spectrosc.* **68,** 362–366 (2014).
34. Chen, Y. *et al.* Study of aluminum particle combustion in solid propellant plumes using digital in-line holography and imaging pyrometry. *Combust. Flame* **182,** 225–237 (2017).
35. Mallery, C. F. & Thynell, S. T. Species and Temperature Profiles of Propellant Flames Obtained from FTIR Absorption Spectroscopy. *Combust. Sci. Technol.* **122,** 113–129 (1997).
36. Vanderhoff, J. A., Teague, M. W. & Kotlar, A. J. Absorption Spectroscopy through the Dark Zone of Solid Propellant Flames. (1992).
37. Anderson, W. R., Meagher, N. E. & Vanderhoff, J. A. Dark zones of solid propellant flames: Critically assessed datasets, quantitative model comparison, and detailed chemical analysis. *Combust. Flame* **158,** 1228–1244 (2011).
38. Eckbreth, A. C., Bonczyk, P. A. & Verdieck, J. F. Combustion diagnostics by laser Raman and fluorescence techniques. *Prog. Energy Combust. Sci.* **5,** 253–322 (1979).

39. Fuest, F. *et al.* Quantitative acetylene measurements in laminar and turbulent flames using 1D Raman/Rayleigh scattering. *Combust. Flame* **162,** 2248–2255 (2015).
40. Parr, T. & Hanson-Parr, D. Cyclotetramethylene tetranitramine/glycidyl azide polymer/butanetriol trinitrate propellant flame structure. *Combust. Flame* **137,** 38–49 (2004).
41. File:CARS diagram.png - Wikimedia Commons. Available at: https://commons.wikimedia.org/wiki/File:CARS_diagram.png. (Accessed: 26th March 2018)
42. Harris, L. E. & Mcllwain, M. E. Coherent Anti-Stokes Raman (CARS) Temperature Measurements in a Propellant Flame.
43. *Laser Diagnostics for Combustion Temperature and Species - Alan C. Eckbreth - Google Books*.
44. Aron, K. & Harris, L. E. CARS Studies of Nitramine Lova Propellant Combustion. (1983).
45. Kearney, S. P. & Guildenbecher, D. R. Temperature measurements in metalized propellant combustion using hybrid fs/ps coherent anti-Stokes Raman scattering. *Appl. Opt.* **55,** 4958 (2016).
46. Hoffmeister, K. N. G., Guildenbecher, D. R. & Kearney, S. P. Hybrid fs/ps CARS for Sooting and Particle-laden Flames. doi:10.2514/6.2016-0282
47. Crosley, D. R. & Smith, G. P. Laser-Induced Fluorescence Spectroscopy For Combustion Diagnostics. *Opt. Eng.* **22,** 225545 (1983).
48. Singla, G., Scouflaire, P., Rolon, C. & Candel, S. Planar laser-induced fluorescence of OH in high-pressure cryogenic LOx/GH2 jet flames. *Combust. Flame* **144,** 151–169 (2006).
49. Donbar, J. M., Driscoll, J. F. & Carter, C. D. Reaction zone structure in turbulent nonpremixed jet flames—from CH-OH PLIF images. *Combust. Flame* **122,** 1–19 (2000).
50. Lee, M. P., McMillin, B. K. & Hanson, R. K. Temperature measurements in gases by use of planar laser-induced fluorescence imaging of NO. *Appl. Opt.* **32,** 5379 (1993).
51. Bucher, P., Yetter, R. A., Dryer, F. L., Parr, T. P. & Hanson-Parr, D. M. PLIF species and ratiometric temperature measurements of aluminum particle combustion in O2, CO2 and N2O oxidizers, and comparison with model calculations. *Symp. Combust.* **27,** 2421–2429 (1998).
52. Smooke, M. D., Yetter, R. A., Parr, T. P. & Hanson-Parr, D. M. Experimental and modeling studies of two-dimensional ammonium perchlorate diffusion flames. *Proc. Combust. Inst.* **28,** 839–846 (2000).
53. Miller, J. D. *et al.* Investigation of transient ignition processes in a model scramjet pilot cavity using simultaneous 100 kHz formaldehyde planar laser-induced fluorescence and CH* chemiluminescence imaging. *Proc. Combust. Inst.* **36,** 2865–2872 (2017).
54. Michael, J. B. *et al.* 100 kHz thousand-frame burst-mode planar imaging in turbulent flames. *Opt. Lett.* **39,** 739 (2014).
55. Ma, L. *et al.* Comparison of 2D and 3D flame topography measured by planar laser-induced fluorescence and tomographic chemiluminescence. *Appl. Opt.* **55,** 5310 (2016).

56. Jiang, N. & Lempert, W. R. Ultrahigh-frame-rate nitric oxide planar laser-induced fluorescence imaging. *Opt. Lett.* **33,** 2236 (2008).
57. Aldén, M., Goldsmith, J. E. M. & Westblom, U. Two-photon-excited stimulated emission from atomic oxygen in flames and cold gases. *Opt. Lett.* **14,** 305 (1989).
58. Goldsmith, J. E. M. Photochemical effects in 205-nm, two-photon-excited fluorescence detection of atomic hydrogen in flames. *Opt. Lett.* **11,** 416 (1986).
59. Niemi, K., Gathen, V. S. der & Döbele, H. F. Absolute calibration of atomic density measurements by laser-induced fluorescence spectroscopy with two-photon excitation. *J. Phys. D. Appl. Phys.* **34,** 2330–2335 (2001).
60. Kulatilaka, W. D., Gord, J. R., Katta, V. R. & Roy, S. Photolytic-interference-free, femtosecond two-photon fluorescence imaging of atomic hydrogen. *Opt. Lett.* **37,** 3051 (2012).
61. Rensberger Weiland, K. J., Wise, M. L. & Smith, G. P. Laser-induced fluorescence detection strategies for sodium atoms and compounds in high-pressure combustors. *Appl. Opt.* **32,** 4066 (1993).
62. Kohse-Höinghaus, K. Laser techniques for the quantitative detection of reactive intermediates in combustion systems. *Prog. Energy Combust. Sci.* **20,** 203–279 (1994).
63. Goldsmith, J. E. M., Anderson, R. J. M. & Williams, L. R. Time-resolved two-photon-excited fluorescence detection of atomic hydrogen in flames. *Opt. Lett.* **15,** 78 (1990).
64. Goldsmith, J. E. M. Two-step saturated fluorescence detection of atomic hydrogen in flames. *Opt. Lett.* **10,** 116 (1985).
65. Lucht, R. P., Salmon, J. T., King, G. B., Sweeney, D. W. & Laurendeau, N. M. Two-photon-excited fluorescence measurement of hydrogen atoms in flames. *Opt. Lett.* **8,** 365 (1983).
66. Kulatilaka, W. D., Patterson, B. D., Frank, J. H. & Settersten, T. B. Comparison of nanosecond and picosecond excitation for interference-free two-photon laser-induced fluorescence detection of atomic hydrogen in flames. *Appl. Opt.* **47,** 4672 (2008).
67. Kulatilaka, W. D., Gord, J. R., Katta, V. R. & Roy, S. Photolytic-interference-free, femtosecond two-photon fluorescence imaging of atomic hydrogen. *Opt. Lett.* **37,** 3051 (2012).
68. Jaggers, H. C. & von Engel, A. The effect of electric fields on the burning velocity of various flames. *Combust. Flame* **16,** 275–285 (1971).
69. Kim, H. H., Takashima, K., Katsura, S. & Mizuno, A. Low-temperature NO_x reduction processes using combined systems of pulsed corona discharge and catalysts. *J. Phys. D. Appl. Phys.* **34,** 604–613 (2001).
70. Ju, Y. & Sun, W. Plasma assisted combustion: Dynamics and chemistry. *Prog. Energy Combust. Sci.* **48,** 21–83 (2015).
71. Stockman, E. S., Zaidi, S. H., Miles, R. B., Carter, C. D. & Ryan, M. D. Measurements of combustion properties in a microwave enhanced flame. *Combust. Flame* **156,** 1453–1461 (2009).
72. Michael, J. B., Chng, T. L. & Miles, R. B. Sustained propagation of ultra-lean methane/air flames with pulsed microwave energy deposition. *Combust. Flame* **160,** 796–807 (2013).
73. Hsu, L.-J. *et al.* Sodium and Potassium Released from Burning Particles of Brown Coal and Pine Wood in a Laminar Premixed Methane Flame Using Quantitative Laser-Induced Breakdown Spectroscopy. *Appl. Spectrosc.* **65,** 684–691 (2011).

74. Weiland, K. J., Wise, M. L. & Smith, G. P. Laser-induced fluorescence detection strategies for sodium atoms and compounds in high-pressure combustors. *Appl. Opt.* **32,** 4066–4073 (1993).
75. Allen, J. E., Anderson, W. R., Crosley, D. R. & Fansler, T. D. Energy transfer and quenching rates of laser-pumped electronically excited alkalis in flames. *Symp. Combust.* **17,** 797–809 (1979).
76. Amorim, J., Baravian, G., Touzeau, M. & Jolly, J. Two-photon laser induced fluorescence and amplified spontaneous emission atom concentration measurements in O_2 and H_2 discharges. *J. Appl. Phys.* **76,** 1487–1493 (1994).
77. Amorim, J., Baravian, G. & Jolly, J. Laser-induced resonance fluorescence as a diagnostic technique in non-thermal equilibrium plasmas. *J. Phys. D. Appl. Phys.* **33,** R51–R65 (2000).
78. Zhao, Y., Li, X. & Ma, L. Multidimensional Monte Carlo model for two-photon laser-induced fluorescence and amplified spontaneous emission. *Comput. Phys. Commun.* **183,** 1588–1595 (2012).
79. Shampine, L. F. Solving Hyperbolic PDEs in Matlab. (2005).
80. Hartung, G. *et al.* A flat flame burner for the calibration of laser thermometry techniques. *Meas. Sci. Technol.* **17,** 2485–2493 (2006).
81. Cheetah 8.0. Available at: https://pls.llnl.gov/people/divisions/materials-science-division/cheetah-8.0. (Accessed: 26th March 2018)
82. Zhu, K., Barkley, S., Dedic, C. E., Sippel, T. & Michael, J. B. Two-photon laser-induced fluorescence imaging of CW microwave-enhanced sodium-doped propellant flames. doi:10.2514/6.2018-1777
83. Zhu, K., Dedic, C. E. & Michael, J. B. Sodium two-photon laser-induced fluorescence characterization with nanosecond and femtosecond excitation. doi:10.2514/6.2017-0259
84. Van Calcar, R. A. *et al.* Saturation of sodium fluorescence in a flame irradiated with a pulsed tunable dye laser. *J. Quant. Spectrosc. Radiat. Transf.* **21,** 11–18 (1979).
85. Lowe, D. G. Object Recognition from Local Scale-Invariant Features. Corfu (1999).
86. Miles, R. B. et al. Plasma-Enhanced Hypersonic Performance Enabled by MHD Power Extraction. doi:10.2514/6.2005-561
87. Rosa, R. J., Krueger, C. H. & Shioda, S. Plasmas in MHD power generation. IEEE Trans. Plasma Sci. 19, 1180–1190 (1991).
88. Cheng, S., Zimmermann, M. & Miles, R. B. Separation of time-averaged turbulence components by laser-induced fluorescence. Phys. Fluids 26, 874 (1983).
89. Mosburger, M., Sick, V. & Drake, M. C. Quantitative high-speed burned gas temperature measurements in internal combustion engines using sodium and potassium fluorescence. Appl. Phys. B 110, 381–396 (2013).

APPENDIX A. LABVIEW PROGRAM FOR BOXCAR INTEGRATOR

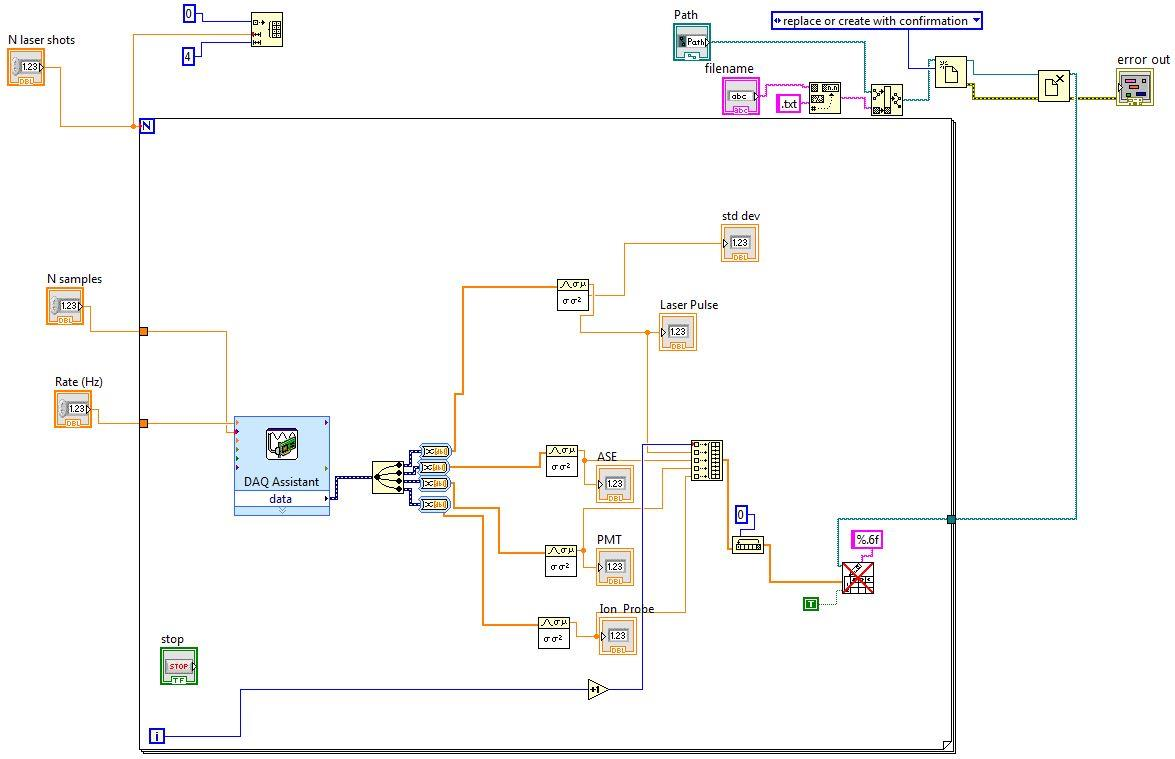

Figure A.1 *LabView data acquisition program block diagram for 4 channels boxcar integrator*

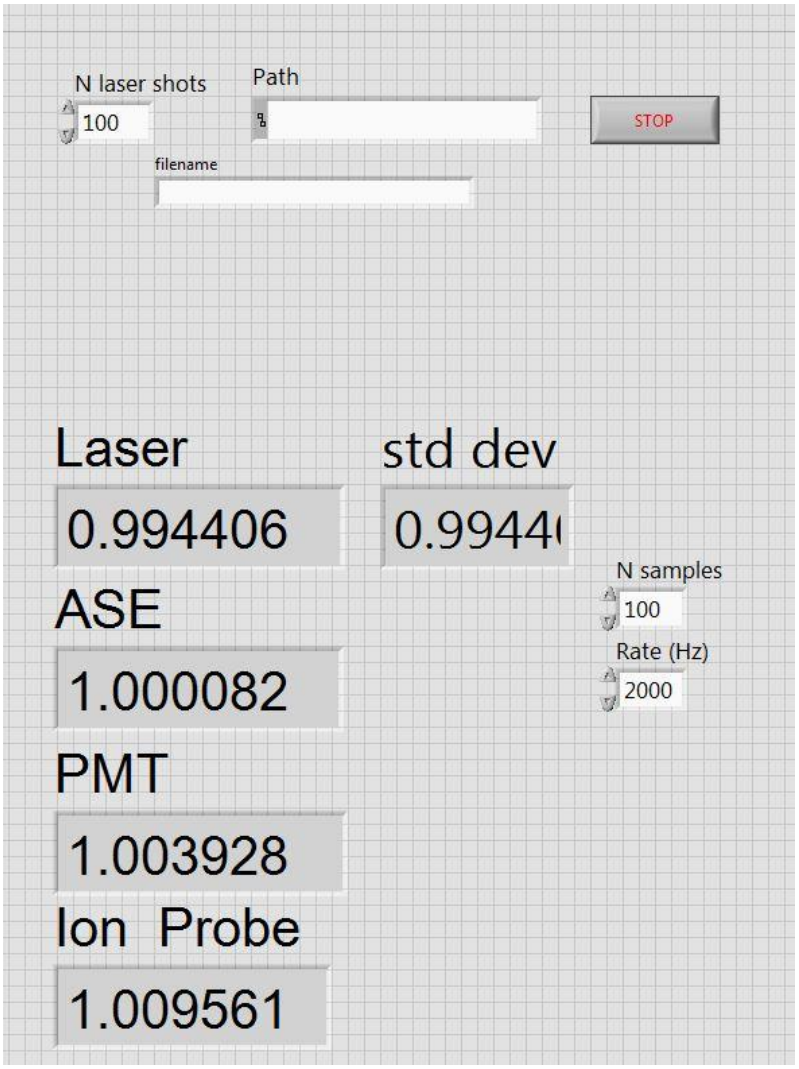

Figure A.2 *LabView data acquisition program front panel for 4 channels boxcar integrator*

APPENDIX B. WR430 TEST SECTION

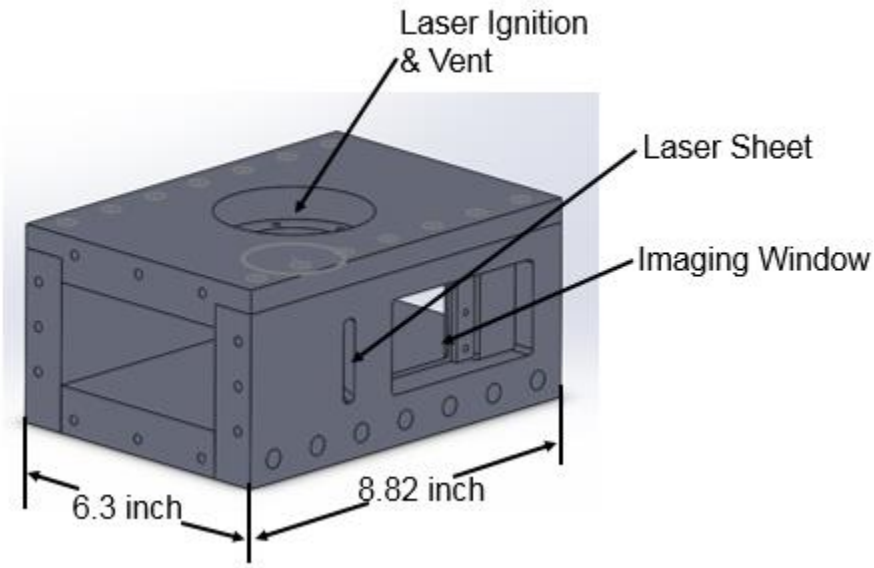

Figure B.1 *Modified WR430 test section in this experiment*

APPENDIX C. SIFT IMAGE REGISTRATION MATLAB CODE

```
clear all; clc; close all
Img_1 = Image_1(:,:,10);  % One camera target Image
Img_1_bs = bitshift(Img_1,2);
Img_1_bgsub = medfilt2(Img_1_bs,[9, 9]); % Image smooth
Img_1_bi = imbinarize(Img_1_bgsub, 0.2); % image
binarized
bw = Img_1_bi;
Img_2 = imread('register_4.tif', 3);   % Another camera
target image
Img_2 = fliplr(Img_2);
Img_2 = bitshift(Img_2, 6);
Img_2 = medfilt2(Img_2,[5, 5]);
%%
Img_2_bi = imbinarize(Img_2, 0.1); % image binarized
Img_2_fl = Img_2_bi(100:700, 100:700); % crop image,
usually need flip images
%% detect features by using SIFT
ptsOriginal  = detectSURFFeatures(bw);
ptsDistorted = detectSURFFeatures(Img_2_fl);
[featuresOriginal,validPtsOriginal] =
extractFeatures(bw,ptsOriginal);
[featuresDistorted,validPtsDistorted] =
extractFeatures(Img_2_fl,ptsDistorted);
%% match features
index_pairs =
matchFeatures(featuresOriginal,featuresDistorted);
matchedPtsOriginal  = validPtsOriginal(index_pairs(:,1));
matchedPtsDistorted =
validPtsDistorted(index_pairs(:,2));figure;
showMatchedFeatures(bw,Img_2_fl,matchedPtsOriginal,matche
dPtsDistorted);
title('Matched SURF points,including outliers');
%% Exclude the outliers, and compute the transformation
matrix
[tform,inlierPtsDistorted,inlierPtsOriginal] =
estimateGeometricTransform(matchedPtsDistorted,matchedPts
Original, 'similarity');
figure; showMatchedFeatures(bw,Img_2_fl,
inlierPtsOriginal,inlierPtsDistorted);
title('Matched inlier points');
outputView = imref2d(size(bw));
Ir = imwarp(Img_2_fl,tform,'OutputView',outputView);
figure; imshowpair(bw, Ir)
save('Tform_1.mat', 'tform')
```